Computational Fluid Dynamics Simulations of Ammonia Catalytic Crackers in OpenFOAM

University of Turku
Department of Mechanical Engineering
Master of Science (Tech) Thesis
Mechanical Engineering
June 2025
Muhammmad Rameez Hashmi

UNIVERSITY OF TURKU
Department of Mechanical Engineering

Muhammmad Rameez Hashmi: Computational Fluid Dynamics Simulations of Ammonia Catalytic Crackers in OpenFOAM

Master of Science (Tech) Thesis, 51 p., 3 app. p.
Mechanical Engineering
June 2025

Ammonia is widely recognised as a promising hydrogen carrier, but efficient catalytic decomposition is required to release hydrogen for clean energy applications. This thesis investigates the catalytic cracking of ammonia through computational fluid dynamics (CFD) simulations. A one-dimensional (1D) plug-flow reactor model was implemented in OpenFOAM and validated against an equivalent Cantera simulation to ensure correct kinetic representation. A more detailed two-dimensional (2D) axisymmetric CFD model of a tubular ammonia cracker was then developed in OpenFOAM to capture radial gradients and transport phenomena. Kinetic mechanisms for ammonia decomposition on ruthenium and nickel catalysts were examined, and the Ru-based mechanism was selected for the 1D/2D simulations in OpenFOAM. The 2D model incorporates multicomponent diffusion and thermal diffusion (Soret effect), enabling it to resolve concentration and temperature gradients neglected by the 1D model. Comparison of 1D and 2D results indicates that the idealised 1D approach slightly overestimates ammonia conversion, whereas the 2D model predicts lower conversion due to pronounced radial gradients. Inclusion of mixture-averaged diffusion and the Soret effect further shapes species and temperature fields, driving hydrogen towards cooler regions and influencing local reaction rates.

Keywords: ammonia decomposition; CFD; OpenFOAM; catalytic reactor; multicomponent diffusion; thermal diffusion; Cantera

Contents

List of Figures

List of Tables

Declaration on use of generative AI

ChatGPT was used to optimize the grammar, tone and clarity of this thesis. Additionally, some of the scripts made in Python for assistance with code generation, particularly in post-processing.

1 Introduction

In the following, an introduction and motivation for research on ammonia decomposition reactions is given. Subsequently, the fundamental aspects of catalytic surface reactions are introduced, followed by the scope of this thesis.

1.1 Motivation and background

The interest in hydrogen as an energy source has been growing consistently in recent years [1]. With its clean emission and high combustion enthalpy of 142 MJ/kg, it can be a useful alternative to traditional fossil-fuel based energy sources. Despite its potential as an energy source, however, there are some key issues pertaining to hydrogen's economic feasibility as an energy source, the most paramount of which is storage and transport. Since it is difficult to liquefy hydrogen and its relatively high flammability, using hydrogen directly as a fuel is problematic [2]. These issues incentivize the use of a hydrogen carrier such as ammonia.

Ammonia is considered an excellent hydrogen carrier because of its high hydrogen content (17.8 % by weight) and because it is significantly easier to liquefy (0.8 MPa and 298 K) [2]. Moreover, the decomposition of ammonia into its constituent gases of nitrogen and hydrogen does not produce carbon oxides, further increasing its attractiveness, in the context of clean energy.

Commercially, the ammonia synthesis reaction has been extensively researched due to its usage in the Haber-Bosch process, in the production of fertilisers. However, the current research has been directed towards the ammonia decomposition reaction, exploring efficient catalysts, reaction kinetics, reactor designs, and optimized conditions for max-

imizing hydrogen yield, minimizing energy consumption, and enhancing overall process sustainability. Experimental analysis and numerical simulation methods can be used to study various aspects of the decomposition reaction and gain valuable insights. Numerical methods can give faster and cheaper insights into various aspects, especially when compared to experimental analyses [1].

1.2 Objectives and scope of this thesis

The objectives of the present thesis are to explore the ammonia decomposition reaction over a catalyst using 1D and 2D simulation techniques. The thesis builds upon a suitable 1D reactor model and then extends these results into a 2D domain and analyses the results from both these simulations.

The research questions that are addressed in this thesis are as follows:

1. How accurately can the ammonia decomposition reaction kinetics, specifically the catalytic mechanisms involving ruthenium and nickel catalysts, be validated using a simplified one-dimensional Plug Flow Reactor (PFR) model in Cantera compared to more detailed Computational Fluid Dynamics (CFD) simulations conducted in OpenFOAM?

2. What are the critical differences in species transport phenomena, reaction kinetics, and thermal profiles between simplified one-dimensional PFR simulations and the more realistic two-dimensional axisymmetric CFD simulations, which incorporate multi-component diffusion and the Soret effect?

3. How do diffusion phenomena influence the radial and axial profiles of species concentrations, temperature gradients, and overall ammonia conversion efficiency in a cylindrical catalytic reactor modelled using OpenFOAM?

2 Literature Review

The literature review of this thesis focuses on two primary aspects:

1. The current understanding of catalyst behaviour for ammonia decomposition is based on how this knowledge is incorporated into computational models.

2. The development and application of CFD methods for simulating catalytic reactors, with particular emphasis on OpenFOAM implementations.

By combining key findings from these two research areas, this review identifies significant research gaps and potential directions for future work, particularly in the context of developing CFD simulations using OpenFOAM to model ammonia decomposition.

2.1 Ammonia decomposition reaction

This section analyses the fundamental reaction of ammonia's decomposition into nitrogen and hydrogen in the context of reaction kinetics, catalytic mechanisms, and thermodynamics, serving as the foundation for the CFD simulations.

The decomposition of ammonia to nitrogen and hydrogen is represented by the following reaction [3]:

$$\mathrm{NH_3} \rightarrow \frac{1}{2}\mathrm{N_2} + \frac{3}{2}\mathrm{H_2} \tag{2.1}$$

with a standard enthalpy change of:

$$\Delta H^\circ = 46.1 \text{ kJ/mol} \tag{2.2}$$

This endothermic reaction is thermodynamically favourable at elevated temperatures. Moreover, the Gibbs free energy of the reaction becomes negative above temperatures of approximately 600 K (327°C) [3]. However, the reaction rate at such temperatures is negligible without a catalyst, highlighting the importance of catalytic materials in practical applications [4]. The thermodynamic equilibrium of ammonia decomposition is influenced by three main factors:

1. **Temperature:** Higher temperatures favour ammonia decomposition, and a nearly total transformation is theoretically achievable at atmospheric pressure above 450°C [3].

2. **Pressure:** Le Chatelier's principle states that a decrease in pressure favours the decomposition reaction by increasing the number of gas molecules [5].

3. **Concentration:** The removal of product gases (H_2 and N_2) from the reaction zone shifts the equilibrium towards further decomposition, which is particularly advantageous in membrane reactor configurations [6].

The thermodynamic constraints involved in the decomposition of ammonia require careful reactor design and precise control of operating conditions to achieve high conversion. Computational Fluid Dynamics (CFD) simulations can play an important role in optimizing these parameters by predicting temperature and concentration gradients in reactors.

2.2 Reaction kinetics

The kinetics of ammonia decomposition are complex and highly dependent on the choice of catalyst. The overall reaction rate is typically described using power-law expressions or more detailed microkinetic models. Each of these models differ in their assumptions and complexity. The primary models for describing the reaction kinetics include:

2.2.1 Power-law (empirical) kinetic models

Power-law models are empirical expressions that relate the reaction rate to the partial pressures of reactants and products. The reaction rate equation for ammonia decomposition is expressed as:

$$r_{\mathrm{NH_3}} = k \cdot P_{\mathrm{NH_3}}^{\alpha} \cdot P_{\mathrm{H_2}}^{\beta} \cdot P_{\mathrm{N_2}}^{\gamma} \tag{2.3}$$

where k is the rate constant, $P_{\mathrm{NH_3}}$, $P_{\mathrm{H_2}}$, and $P_{\mathrm{N_2}}$ are the partial pressures of ammonia, hydrogen, and nitrogen, respectively. The exponents α, β, and γ are the reaction orders with respect to NH_3, H_2, and N_2, respectively. These reaction orders are determined experimentally and can vary depending on the catalyst and operating conditions [7].

2.2.2 Langmuir–Hinshelwood (L–H) model

L–H models are mechanistic and consider the adsorption of reactants on the catalyst surface, followed by surface reactions. The equation for the reaction rate of ammonia decomposition may be expressed as:

$$r_{\mathrm{NH_3}} = \frac{k\left(P_{\mathrm{NH_3}}^2 - \frac{P_{\mathrm{N_2}}\,P_{\mathrm{H_2}}^3}{K_P}\right)}{\left(1 + \sqrt{K_{\mathrm{NH_3}}\,P_{\mathrm{N_2}}^2\,P_{\mathrm{H_2}}^3}\right)^2} \tag{2.4}$$

where K_P is the equilibrium constant of pressure, and $K_{\mathrm{NH_3}}$ is the equilibrium constant of adsorption [8].

These models assume that the surface reaction is the rate-determining step. They provide an accurate description for simple catalytic systems, especially under varying pressures and temperatures. For instance, Armenise *et al.* [9] developed an L–H model that effectively predicted ammonia conversion in integral reactors.

2.2.3 Langmuir–Hinshelwood–Hougen–Watson (LHHW) model

Langmuir–Hinshelwood–Hougen–Watson (LHHW) models incorporate the mechanistic treatment of L–H models with empirical modifications to accommodate experimental

findings. A closed-form rate expression is developed, and an iterative refinement is used to fit experimental data to the equation. LHHW models are versatile and have been applied in simulating ammonia decomposition over a range of catalysts, from Ru- to Ni-based systems [10].

The LHHW method entails the derivation of kinetic expressions by systematically taking each elementary reaction step as the rate-determining step while assuming that other steps are in a quasi-equilibrium state. This approach provides mechanistic insight by identifying the most statistically probable rate-determining step based on empirical data fitting. As a result, it is particularly suitable for modelling complex catalytic systems, such as ammonia decomposition on ceria-supported Ni-Ru catalysts [10].

2.2.4 Temkin–Pyzhev model

This semi-empirical model assumes that the desorption of nitrogen is the rate-determining step for NH_3 decomposition. The model accounts for surface coverage effects and is expressed as:

$$r_{\mathrm{NH_3}} = k \left[\left(\frac{P_{\mathrm{NH_3}}^2}{P_{\mathrm{H_2}}^3} \right)^{\beta} - \frac{P_{\mathrm{N_2}}}{k_{\mathrm{eq}}^2} \left(\frac{P_{\mathrm{H_2}}^3}{P_{\mathrm{NH_3}}^2} \right)^{1-\beta} \right] \tag{2.5}$$

where β is the decomposition reaction index, and k_{eq} is the equilibrium constant of the reaction [11].

The Temkin–Pyzhev model is particularly useful in cases where the catalyst surface is heterogeneous in energy and the availability of adsorption sites. Conventional models such as the Langmuir–Hinshelwood hypothesis assume uniform adsorption sites, which may not accurately represent real catalyst surfaces. The Temkin–Pyzhev model addresses this by introducing the reaction index β, which accounts for the variability in adsorption energies across different sites. This leads to a more accurate description of reaction kinetics on heterogeneous surfaces, where adsorbate–adsorbate interactions and site-dependent affinities significantly influence the reaction rate.

2.2.5 Stepwise decomposition of ammonia

The ammonia molecule undergoes stepwise decomposition on the active site by successively breaking down into NH_2, NH, and finally atomic nitrogen, releasing hydrogen atoms at each step. The nitrogen and hydrogen atoms then pair to form N_2 and H_2 molecules, respectively, which subsequently desorb into the gas phase [8]. The reaction proceeds as follows, where $\cdot$ denotes a catalytic site [8]:

Adsorption step

$$2\,NH_3 + 2\,\cdot \longrightarrow 2\,NH_3\cdot$$

Surface reaction steps

$$2\,NH_3\cdot + 2\,\cdot \longrightarrow 2\,NH_2\cdot + 2\,H\cdot$$

$$2\,NH_2\cdot + 2\,\cdot \longrightarrow 2\,NH\cdot + 2\,H\cdot$$

$$2\,NH\cdot + 2\,\cdot \longrightarrow 2\,N\cdot + 2\,H\cdot$$

Nitrogen desorption

$$2\,N\cdot \longrightarrow N_2 + 2\,\cdot$$

Hydrogen desorption

$$6\,H\cdot \longrightarrow 3\,H_2 + 6\,\cdot$$

For each discrete step of the reaction, a kinetic expression can be derived to describe the rate of the process in both the forward and reverse directions. These rates depend on the rate constants and the concentrations or surface coverages of the participating reactants. This leads to a set of differential equations aimed at assessing the overall reaction rate. Simplifying assumptions, such as the steady-state approximation—where no net accumulation of surface intermediates is expected—are often applied [12].

These models are commonly validated by comparison with experimental data. For instance, Kulkarni *et al.* employed *ab initio* calculations to develop microkinetic models

of ruthenium catalysts, identifying the rate-determining step and achieving satisfactory agreement with experimental observations.

2.2.6 Summary of kinetic models

In conclusion, the discussed models represent a distinct trade-off between simplicity and mechanistic complexity. Power-law models are simple to apply and convenient for initial reactor design but provide limited insight into the reaction mechanism. The Langmuir–Hinshelwood and LHHW models address this limitation by incorporating surface reaction and adsorption phenomena, thereby improving predictability over a range of conditions, albeit with added assumptions. The Temkin–Pyzhev model offers a middle ground by accounting for surface heterogeneity without the full complexity of a mechanistic treatment. Finally, microkinetic models provide the most comprehensive description by considering all elementary steps and surface intermediates but require extensive experimental or computational effort.

2.3 Catalyst research for ammonia decomposition

This section reviews the current state of catalyst research for ammonia decomposition, focusing on different catalyst types, support materials, and performance metrics.

2.3.1 Ruthenium

Ruthenium (Ru) is widely recognized as the most active metal for ammonia decomposition at relatively moderate temperatures (300–500°C) [13]. The superior performance of Ru catalysts is attributed to their optimal nitrogen binding energy, which facilitates both the breaking of N–H bonds and the recombination of nitrogen atoms without excessive binding that would inhibit product desorption [14].

Several studies have investigated the performance of Ru catalysts supported on various materials. For example, Su *et al.* [14] delineated the progress of research on Ru-based catalysts for ammonia decomposition to produce hydrogen. Their review indicated that

Ru supported on carbon nanotubes (CNTs) exhibits high activity due to electronic interactions between Ru and the CNT support. The performance of Ru/CNT catalysts is highly sensitive to particle size, with 3–5 nm diameter particles being optimal [14].

The activity of Ru catalysts can also be enhanced by the addition of promoters. Alkali metals, particularly cesium (Cs) and potassium (K), improve the performance of the Ru catalyst by donating electrons to the Ru particles, which facilitates the rate-determining nitrogen recombination step [14]. However, the high cost and limited availability of Ru have motivated the search for alternative catalytic materials [13].

Moreover, Zhang *et al.* [15] developed a detailed microkinetic reaction mechanism for ammonia synthesis using Ba-promoted Ru catalysts supported on yttria-stabilized zirconia (YSZ). The mechanism is based on the work by Hinrichsen *et al.* [16], who experimentally produced results of ammonia's reaction and decomposition. Their mechanism consists of twelve elementary reactions, six for ammonia synthesis and six for ammonia decomposition. Additionally, the mechanism covers adsorption, desorption, surface reactions, and recombination processes for nitrogen, hydrogen, and ammonia. The inclusion of reverse reactions allows the mechanism to simulate both decomposition and synthesis. Zhang *et al.* [15] also provided CHEMKIN-format mechanism files, making their work applicable to CFD simulations using platforms such as Cantera or OpenFOAM.

2.3.2 Nickel

Nickel (Ni) has also been investigated as a more economical alternative to Ru, especially for operation at higher temperatures (above 500°C) [17]. Takahashi and Fujitani [18] conducted a comparative study of Ru and Ni catalysts, concluding that although Ni requires higher operating temperatures, it remains a viable option for large-scale applications. The effectiveness of nickel catalysts is highly dependent on the support material and preparation methods.

While Ni supported on alumina (Al_2O_3) is common, recent studies have explored supports like ceria (CeO_2) and zirconia (ZrO_2) to enhance catalytic activity [2]. Lucentini *et al.* [10] examined a Ni–Ru bimetallic catalyst supported in CeO_2, demonstrating

synergistic effects that outperform single metal catalysts.

In terms of simulation, Appari *et al.* [19] developed a detailed surface reaction mechanism in CHEMKIN format for ammonia decomposition on Ni. Their model, validated for temperatures between 700 and 1500 K and pressures from 5.3 Pa to 100 kPa, has also been used in simulations of solid oxide fuel cells powered by ammonia [19].

2.3.3 Cobalt

Cobalt (Co) catalysts have also been considered. Lendzion-Bielun *et al.* [20] demonstrated that Co-based catalysts can achieve good activity, especially when enhanced with alkali metal promoters or paired with suitable supports. The temperature range that was studied was 500°C to 550°C [20]. Recent studies have focused on improving Co catalyst performance through barium (Ba) promotion. Almisbaa and Sautet [21] showed through theoretical analysis that Ba significantly enhances cobalt catalyst activity by altering the electronic properties of active sites. Gunnarson *et al.* [22] combined computational modelling and experimental validation to develop a cost-effective, high-performance Co–Ba catalyst that nearly matches Ru-based systems.

2.3.4 Iron

Iron (Fe) catalysts have also been explored. Yeo *et al.* [23], for instance, studied the decomposition of ammonia on a Fe (100) surface using density functional theory (DFT), revealing the fundamental reaction steps on iron surfaces. Lanzani and Laasonen [24] investigated the decomposition of ammonia in nano-sized iron clusters, showing that these clusters can outperform bulk iron in catalytic activity. Arabczyk and Zamłynny [25] also did experiments by investigating iron catalysts over ammonia decomposition; their temperature range was found to be 325°C to 500°C.

2.3.5 Non-metal catalysts

Although metal catalysts dominate ammonia decomposition research, non-metal catalysts have also been studied. Makepeace *et al.* [26] investigated non-stoichiometric lithium

imide as a catalyst, finding that it outperforms sodium amide and even some Ru and Ni-based catalysts under certain conditions. Their work highlighted the importance of intermediate stoichiometry between lithium imide and lithium amide.

In another study, Makepeace *et al.* [27] also studied lithium–calcium imide catalysts, expanding the range of effective non-metal catalysts. These studies suggest that various metal amide-based materials could offer promising ammonia decomposition activity, potentially involving different reaction mechanisms.

Wood *et al.* [28] conducted isotopic studies on sodium amide-catalyzed ammonia decomposition. Their findings revealed that the reaction mechanism differs from that of transition-metal catalysts, showing a significant kinetic isotope effect not observed in Ni-catalyzed reactions.

2.4 CFD simulations of ammonia decomposition

CFD simulations for catalytic reactors typically involve solving the conservation equations for mass, momentum, energy, and species transport, coupled with models for chemical reactions. The general approach can be categorized based on how the catalyst is represented in the model:

1. **Pseudo-homogeneous models:** The reactor is treated as a uniform medium, in which catalyst and fluid phases are considered as a single continuum with effective properties. This simplification assumes that the reaction kinetics are volume-averaged and that the catalyst is distributed uniformly within the reactor domain. These models are simple and computationally efficient, but may not capture local phenomena at the catalyst surface. Pseudo-homogeneous models are often used in early-stage feasibility studies or for systems where detailed catalyst structure does not significantly affect global reaction rates [29].

2. **Heterogeneous models:** The catalyst and fluid phases are treated separately, with explicit modelling of interfacial transport processes. The catalyst is represented as a distinct phase, and surface reactions are described through bound-

ary conditions on catalyst surfaces. This approach allows the simulation of adsorption, desorption, and surface reaction kinetics. Heterogeneous models provide more detailed and accurate insights but require greater computational resources. They are well suited for the analysis of catalytic monoliths or packed-bed reactors, where gas-solid interactions and thermal effects significantly influence reactor performance [29].

3. **Resolved catalyst models:** The actual geometry of the catalyst particles or structures is resolved in the computational domain. These models simulate transport phenomena and reactions at the scale of catalyst pores or grains, capturing local effects such as intra-particle diffusion and thermal gradients [30]. Although they provide the most detailed representation, resolved catalyst models are computationally intensive and typically limited to small domains. They are commonly used in conjunction with experimental studies or multiscale modelling frameworks, where microscale results are upscaled to inform reactor-scale simulations [31].

3 Methodology

This section describes the equations used to model the fluid flow within the OpenFOAM framework for the 1D and 2D CFD simulations. It starts by describing the code setup to compare the two published reaction mechanisms for ammonia decomposition by Zhang *et al.* [15] and Appari *et al.* [19] (describing reactions over a ruthenium and nickel catalyst, respectively). It also describes the one-dimensional plug flow reactor used in Cantera which was used to validate the mechanisms. Furthermore, the section also describes the process for discretizing the domain, setting the boundary conditions, implementing the reaction mechanisms in OpenFOAM. OpenFOAM version 9 was used as it was compatible with the catalyticFoam, developed by Maestri and Cuoci [32].

3.1 Governing equations for fluid flow

The fluid flow within the catalytic reactor is governed by the conservation equations for mass and momentum. For a compressible, Newtonian fluid in an axisymmetric coordinate system (x, r), where x represents the axial coordinate and r the radial coordinate, these equations can be expressed as follows:

3.1.1 Conservation of mass

The continuity equation, representing the conservation of total mass, is given by:

$$\frac{\partial \rho}{\partial t} + \frac{\partial}{\partial x}(\rho u) + \frac{1}{r}\frac{\partial}{\partial r}(r\rho v) = 0 \tag{3.1}$$

where ρ is the fluid density, t is time, u is the axial velocity component, and v is the

radial velocity component.

3.1.2 Conservation of momentum

The momentum conservation equations in the axial and radial directions for a compressible, Newtonian fluid are expressed as:

$$\begin{aligned}\frac{\partial}{\partial t}(\rho u) + \frac{\partial}{\partial x}(\rho u u) + \frac{1}{r}\frac{\partial}{\partial r}(r\rho v u) = -\frac{\partial p}{\partial x} + \\ \frac{\partial}{\partial x}\left[\mu\left(2\frac{\partial u}{\partial x} - \frac{2}{3}(\nabla\cdot\mathbf{v})\right)\right] + \frac{1}{r}\frac{\partial}{\partial r}\left[r\mu\left(\frac{\partial u}{\partial r} + \frac{\partial v}{\partial x}\right)\right]\end{aligned} \tag{3.2}$$

$$\begin{aligned}\frac{\partial}{\partial t}(\rho v) + \frac{\partial}{\partial x}(\rho u v) + \frac{1}{r}\frac{\partial}{\partial r}(r\rho v v) = -\frac{\partial p}{\partial r} + \\ \frac{\partial}{\partial x}\left[\mu\left(\frac{\partial v}{\partial x} + \frac{\partial u}{\partial r}\right)\right] + \frac{1}{r}\frac{\partial}{\partial r}\left[r\mu\left(2\frac{\partial v}{\partial r} - \frac{2}{3}(\nabla\cdot\mathbf{v})\right)\right] - \\ 2\mu\frac{v}{r^2} + \frac{2}{3}\frac{\mu}{r}(\nabla\cdot\mathbf{v})\end{aligned} \tag{3.3}$$

where p is the pressure, μ is the dynamic viscosity, and $\nabla\cdot\mathbf{v} = \frac{\partial u}{\partial x} + \frac{1}{r}\frac{\partial}{\partial r}(rv)$ represents the divergence of the velocity field.

The viscous stress terms in these equations account for the momentum diffusion due to molecular transport, whereas the pressure gradient terms represent the forces due to pressure variations within the fluid. For the axisymmetric formulation, additional terms arise due to the cylindrical coordinate system, particularly in the radial momentum equation, where terms containing $\frac{1}{r}$ and $\frac{1}{r^2}$ appear due to the geometric effects of the cylindrical coordinates.

3.1.3 Species transport using mixture-averaged model

The transport of chemical species within the 2D axisymmetric reactor model is governed by the mixture-averaged model as described in Maestri and Cuoci [32]. This model assumes both Fickian and thermal diffusion when evaluating diffusion velocities [32].

The conservation equation for species mass fraction ω_k in a , reacting gas mixture with multiple species is given by:

$$\frac{\partial}{\partial t}(\rho\omega_k) + \nabla \cdot (\rho\omega_k \mathbf{v}) = -\nabla \cdot (\rho\omega_k \mathbf{V}_k) + \dot{\Omega}_k^{\text{hom}}, \quad k = 1, \ldots, N_{\text{CG}} \tag{3.4}$$

where:

- ρ is the gas mixture density,
- ω_k is the mass fraction of species k,
- $\mathbf{v}$ is the velocity vector,
- $\mathbf{V}_k$ is the diffusion velocity of species k,
- $\dot{\Omega}_k^{\text{hom}}$ is the homogeneous chemical source term,
- N_{CG} is the number of gas-phase species.

The diffusion velocity $\mathbf{V}_k$ is defined using the mixture-average approximation and includes both concentration and thermal diffusion effects:

$$\mathbf{V}_k = -\Gamma_k \frac{1}{\omega_k} \nabla\omega_k - \frac{\Gamma_k \vartheta_k}{X_k T} \nabla T \tag{3.5}$$

where:

- Γ_k is the mixture-averaged diffusion coefficient for species k,
- X_k is the mole fraction of species k,
- T is the temperature,
- ϑ_k is the thermal diffusion ratio (accounting for the Soret effect).

To ensure that the total mass flux due to diffusion is zero (i.e., to conserve mass), a correction velocity $\mathbf{V}^C$ is added:

$$\mathbf{V}^C = -\sum_{k=1}^{N_C} \mathbf{V}_k \tag{3.6}$$

The corrected diffusion velocity $\mathbf{V}_k^C$, which satisfies mass conservation, is then:

$$\mathbf{V}_k^C = \mathbf{V}_k + \mathbf{V}^C \tag{3.7}$$

This corrected velocity is substituted into the species transport equation (1) to enforce the condition:

$$\sum_{k=1}^{N_C} \rho\omega_k \mathbf{V}_k^C = 0$$

3.1.4 Energy transport

The conservation of energy in the reactor is described by the following equation:

$$\rho\hat{C}_P\frac{\partial T}{\partial t} + \rho\hat{C}_P\left(u\frac{\partial T}{\partial x} + v\frac{\partial T}{\partial r}\right) = \frac{\partial}{\partial x}\left(\lambda\frac{\partial T}{\partial x}\right) + \frac{1}{r}\frac{\partial}{\partial r}\left(r\lambda\frac{\partial T}{\partial r}\right) - \rho\sum_{k=1}^{N_{CG}}\hat{C}_{P,k}\omega_k\mathbf{V}_k\cdot\nabla T - \sum_{k=1}^{N_{CG}}\hat{H}_k^{hom}\dot{\Omega}_k^{hom} \tag{3.8}$$

where $\hat{C}_P$ is the specific heat capacity of the mixture at constant pressure, λ is the thermal conductivity, $\hat{C}_{P,k}$ is the specific heat capacity of species k, and $\hat{H}_k^{hom}$ is the specific enthalpy of species k.

The first two terms on the right-hand side represent heat conduction according to Fourier's law. The third term accounts for the enthalpy transport as a result of species diffusion, whilst the fourth term represents the heat release or absorption due to chemical reactions.

3.1.5 Lewis number approach

In addition to the mixture-averaged diffusion model, the Lewis number approach was implemented to relate the thermal and mass diffusivities, specifically for the pseudo 1D model. The Lewis number for species k is defined as:

$$Le_k = \frac{\lambda}{\rho \hat{C}_P \Gamma_k} \tag{3.9}$$

where $\frac{\lambda}{\rho \hat{C}_P}$ represents the thermal diffusivity of the mixture. The Lewis number characterises the relative rates of thermal and mass diffusion. For $Le_k = 1$, thermal and mass diffusion occur at the same rate, whilst $Le_k > 1$ indicates that thermal diffusion is faster than mass diffusion, and $Le_k < 1$ indicates the opposite.

3.2 Thermodynamic properties

The thermodynamic and transport properties of the gas mixture are essential for the accurate solution of the governing equations. The density of the mixture is calculated using the ideal gas law:

$$\rho = \frac{p\bar{M}}{RT} \tag{3.10}$$

where $\bar{M}$ is the mean molecular weight of the mixture, R is the universal gas constant, and T is the temperature.

The specific heat capacity of the mixture is calculated as a mass-weighted average of the individual species' specific heat capacities:

$$\hat{C}_P = \sum_{k=1}^{N_{CG}} \omega_k \hat{C}_{P,k} \tag{3.11}$$

3.3 Cantera and 1-D plug flow reactor (PFR)

Cantera is an open-source software toolkit designed to model chemical reactions, thermodynamic properties, and transport phenomena. It enables integration of detailed physical models into simulations and can be used on interfaces such as MATLAB, Python or C/C++ [33].

A plug flow reactor model is a type of model in which the reactor is assumed to be one-dimensional. However, the state of the gas is allowed to change only in the stream-wise

direction, meaning that in the radial and azimuthal directions the gas is homogenous. Another critical assumption of this model is that diffusion is neglected in all directions. Mixing is assumed to occur only in the radial directions, so that the concentrations of the reactants and products are the same at any given axial position along the reactor. Simultaneously, no axial mixing is assumed. In addition, one or more of the interior surfaces can be assumed to be catalytically active, which allows heterogeneous reactions to occur [34].

The ideal gas law from equation 3.11 is used to describe the state of the gas [34].

The net rate at which species are generated can be written by slightly modifying the mass conservation equation (i.e. equation 6) so it becomes:

$$\dot{m}_s = \sum_j \frac{A_{s,j}}{V} \left(\sum_k \dot{s}_{k,j} W_k \right)$$

where:

- $\dot{m}_s$ is the net mass production rate per unit volume due to surface reactions (kg/m^3·s),
- $\dot{s}_{k,j}$ is the net rate of production of species k on surface j (mol/m^2·s),
- W_k is the molecular weight of species k (kg/mol).

The overall mass conservation equation for the reactor can then be written as:

$$u\frac{d\rho}{dz} + \rho\frac{du}{dz} = \dot{m}_s \tag{3.12}$$

where:

- u is the axial velocity of the gas (m/s),
- ρ is the density of the gas (kg/m^3),
- z is the axial coordinate (m).

The momentum conservation and energy balance equations in the streamwise direction are similar to equations 3.2, 3.3 and 3.9 respectively. The conservation equation for each

gas-phase species is given by a simplified version of equation 9:

$$\rho u \frac{dY_k}{dz} = -Y_k \dot{m}_s + \dot{\omega}_k W_k + \sum_j \frac{A_{s,j}}{V} \dot{s}_{k,j} W_k \tag{3.13}$$

where:

- Y_k is the mass fraction of species k,
- W_k is the molecular weight of species k (kg/mol).

Surface species are assumed to be in quasi-steady-state, so their net production rates vanish:

$$\dot{s}_{i,j} = 0 \quad \text{for all surface species } i \neq 0 \tag{3.14}$$

Additionally, the total surface coverage on each surface must satisfy:

$$\sum_i \theta_{i,j} = 1 \tag{3.15}$$

where $\theta_{i,j}$ is the fractional surface coverage of species i on surface j.

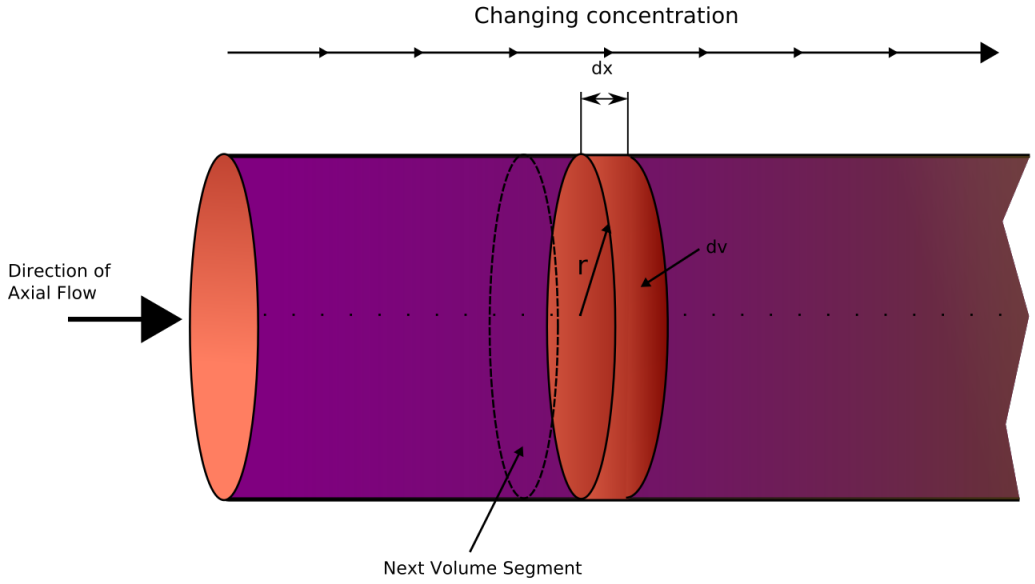

Figure 3.1: Schematic of a plug flow reactor showing an infinitesimal control volume [35]

3.3.1 Implementing Cantera with YAML file

The mechanisms by Zhang *et al.* [15] and Appari *et al.* [19] were used in the Cantera simulations. This was subsequently loaded into a Cantera tutorial that models a plug flow reactor with surface chemistry [36].

It begins by defining reactor geometry, flow velocity, porosity, and suitable temperature and pressure. The gas- and surface-phase chemistries are loaded from a Cantera YAML file. A gas mixture was initialized, and a surface mechanism is applied using ReactorSurface. The reactor is modelled as isothermal and one-dimensional, with a defined surface area-to-volume ratio representing catalytic activity. The simulation integrates along the reactor length, solving for gas-phase and surface species evolution. Results, including mole fractions and surface coverages, were then used for plotting [36].

3.4 OpenFOAM

OpenFOAM (Open Field Operation and Manipulation) is an open-source computational fluid dynamics (CFD) platform widely used for the numerical simulation of fluid flow,

heat transfer, and chemical reactions. Built on the finite volume method, OpenFOAM provides a flexible and extensible framework for solving partial differential equations that arise in continuum mechanics. In the context of catalytic surface reactions, OpenFOAM offers the foundational tools necessary to model and couple fluid dynamics with species transport and surface reaction kinetics [37]. Its object-oriented design allows for the integration of user-defined surface chemistry models and complex boundary conditions, making it suitable for simulating reactive flows over catalytic surfaces. By discretizing both the bulk and surface governing equations on unstructured meshes, OpenFOAM facilitates accurate modelling of the interaction between flowing species and catalytic boundaries [37]. This capability makes OpenFOAM a powerful open source tool for investigating heterogeneous catalysis in industrial and research applications.

3.5 OpenFOAM implementations for catalytic surface reactions

1. **catalyticFoam:** This is a custom CFD solver developed by Maestri and Cuoci [32]. `catalyticFoam` uses an operator-splitting algorithm to decouple surface reaction kinetics from fluid transport. This splitting technique allows for the efficient simulation of catalytic flows with detailed microkinetics in complex geometries by separating the fast surface reactions from the slower fluid transport processes.

2. **catalyticChamberFoamV.1:** This implementation was created by Robledo Asencio *et al.* [38] for modelling the catalytic decomposition of monopropellants in thrusters. It was developed by combining OpenFOAM's `reactingFoam` and `chemFoam` solvers, integrating new dictionaries for species and porous media parameters, as well as heat transfer models with custom coefficients.

3. **surfaceChemistryModels:** This solver integrates a custom library which provides support for various surface reaction rate models. These models enable a detailed simulation of surface chemical mechanisms in porous catalytic media, especially in

packed-bed reactors [39].

4. **catchyCFDEM:** This is an open source CFD-DEM solver based on OpenFOAM and LIGGGHTS, developed to simulate fluidized reactive gas-solid beds with detailed heterogeneous catalysis [40]. It supports multiscale modelling with explicit particle tracking and microkinetic surface chemistry, and includes options ranging from pseudo-homogeneous to fully heterogeneous models with mass transfer.

OpenFOAM implementation	**Developer**	**Source code**
catalyticFoam	Maestri and Cuoci [32]	`https://github.com/multiscale-catalysis-polimi/catalyticFoam`
reactingFoam + chemFoam	OpenFOAM Foundation / ESI	`https://github.com/OpenFOAM/OpenFOAM-6/blob/master/applications/solvers/combustion/reactingFoam/reactingFoam.C` `https://github.com/OpenFOAM/OpenFOAM-4.x/blob/master/applications/solvers/combustion/chemFoam/chemFoam.C`
surfaceChemistryModels	Nguyen *et al.* [39]	`https://github.com/danhnam11/surfaceChemistryModels-8`
catchyCFDEM	Wéry *et al.* [40]	`https://github.com/CFDEMproject/CFDEMcoupling-PUBLIC`

Table 3.1: Source code for OpenFOAM implementations for heterogeneous reacting flow solvers.

3.6 CHEMKIN file description and Arrhenius parameters for ammonia synthesis/decomposition

3.6.1 Zhang *et al.* [15]

The study by Zhang *et al.* [15] provides a detailed microkinetic model for ammonia synthesis over barium-promoted ruthenium catalysts supported on yttria-stabilised zirconia (YSZ), encapsulated in a CHEMKIN-compatible format. As mentioned in the literature review, this model builds upon the mechanism originally developed by Hinrichsen *et*

al. [16] for Cs−Ru/MgO catalysts, but has been significantly modified to represent the Ba−Ru/YSZ system across a wide range of operating conditions, specifically temperatures from 300 °C to 450 °C, inlet H_2/N_2 ratios from 0.1 to 3.0, and pressures from 0 to 10 bar (gauge).

Zhang *et al.* [15] constructed the microkinetic model by combining experimental data with theoretical adjustments to ensure thermodynamic consistency and alignment with observed reaction rates. Experimental measurements were conducted using a tubular reactor configuration, where the Ba−Ru/YSZ catalyst was tested under various temperatures, pressures, and H_2/N_2 stoichiometric ratios. The reaction rates were measured in units of mmol/g_{Ru}/h, with the specific synthesis rate at 400 °C and 1.0 MPa reported as approximately 1410 mmol/g_{Ru}/h. These experimental results provided the basis for fitting the rate parameters [15].

To develop the CHEMKIN file, Zhang *et al.* [15] modified the rate expressions from Hinrichsen *et al.* [16], incorporating coverage-dependent activation energies to capture the dynamic evolution of surface species such as N(Ru) and H(Ru). The rate parameters, including pre-exponential factors (A), temperature exponents (β), and activation energies (E), were empirically adjusted using a least-squares technique to minimise the Gibbs free energy, ensuring microscopic reversibility across the temperature range. Initial estimates for the pre-exponential factors were derived from transition-state theory, with a nominal value of approximately $1 \times 10^{13}\,\mathrm{s}^{-1}$ for first-order surface reactions, as determined by the equation $A = \frac{k_B T}{h} \frac{1}{\Gamma^{n-1}}$, where k_B is the Boltzmann constant, h is the Planck constant, Γ is the ruthenium surface site density ($\Gamma = 2.6 \times 10^{-9}\,\mathrm{mol\,cm}^{-2}$), and n is the reaction order. These parameters were further refined to match the experimental data, particularly to account for the observed hydrogen poisoning effects at lower temperatures and the optimal H_2/N_2 ratios for maximum ammonia synthesis rates [15].

Table 3.2 presents the Arrhenius parameters for the 12-step reaction mechanism used in the CHEMKIN file, as reported by Zhang *et al.* [15]. The table includes the pre-exponential factor (A), temperature exponent (β), and activation energy (E) for each reaction, with units in cm, s, and $\mathrm{kJ\,mol}^{-1}$, respectively. For reactions involving sticking

coefficients (Reactions 1, 3, and 5), the pre-exponential factor is listed as the sticking coefficient value, while for reactions with coverage-dependent activation energies (Reactions 2, 4, 7–9, and 12), the activation energy includes a coverage-dependent term.

Table 3.2: Arrhenius parameters for the microkinetic reaction mechanism of ammonia synthesis over Ba−Ru/YSZ catalysts, as used in the CHEMKIN file by Zhang *et al.* [15].

No.	**Reaction**	A (cm, s)	β	E (kJ mol^{-1})
1	$N_2 + 2\,(Ru) \longrightarrow N(Ru) + N(Ru)$ (sticking coefficient)	2.892×10^{-4}	0.000	38.949
2	$N(Ru) + N(Ru) \longrightarrow N_2 + 2\,(Ru)$	2.015×10^{-17}	-0.279	$148.027 - 14\theta_{N(Ru)}$
3	$H_2 + 2\,(Ru) \longrightarrow H(Ru) + H(Ru)$ (sticking coefficient)	4.007×10^{-2}	0.000	0.0
4	$H(Ru) + H(Ru) \longrightarrow H_2 + 2\,(Ru)$	3.600×10^{-30}	0.658	$91.948 - 2\theta_{H(Ru)}$
5	$NH_3 + (Ru) \longrightarrow NH_3(Ru)$ (sticking coefficient)	1.247×10^{-3}	0.000	0.0
6	$NH_3(Ru) \longrightarrow NH_3 + (Ru)$	2.235×10^{-11}	0.083	83.536
7	$N(Ru) + H(Ru) \longrightarrow NH(Ru) + (Ru)$	8.424×10^{-38}	0.000	$83.620 - 7\theta_{N(Ru)}$
8	$NH(Ru) + (Ru) \longrightarrow N(Ru) + H(Ru)$	6.813×10^{-19}	0.207	$30.972 + 1\theta_{N(Ru)}$
9	$NH(Ru) + H(Ru) \longrightarrow NH_2(Ru) + (Ru)$	4.949×10^{-19}	-0.083	75.236
10	$NH_2(Ru) + (Ru) \longrightarrow NH(Ru) + H(Ru)$	3.886×10^{-19}	-0.083	$15.767 + 1\theta_{N(Ru)}$
11	$NH_2(Ru) + H(Ru) \longrightarrow NH_3(Ru) + (Ru)$	3.886×10^{-19}	0.083	$15.767 + 1\theta_{N(Ru)}$
12	$NH_3(Ru) + (Ru) \longrightarrow NH_2(Ru) + H(Ru)$	3.886×10^{-19}	0.083	$64.980 + 1\theta_{N(Ru)}$

3.6.2 Appari *et al.* [19].

Appari *et al.* [19], in his research, presented and validated a detailed surface reaction mechanism for ammonia decomposition over a nickel catalyst [19]. Their mechanism was based on the unity bond index quadratic exponential potential (UBI-QEP) method. Their mechanism developed consists of two main components, the first of which focused on the catalytic decomposition of ammonia and included twelve elementary reactions involving three gas-phase species and five adsorbed surface intermediates. The second component incorporated additional reactions related to hydrogen oxidation, enabling the mechanism's applicability to direct ammonia solid oxide fuel cells (SOFCs). These hydrogen oxidation steps (R13–R22) are adapted from the work of Janardhanan and Deutschmann

[41]. The parameters from Janardhanan and Deutschmann [41] were slightly modified for thermodynamic consistency. However, ammonia decomposition can be modelled using just reactions 1 through 12 [19].

Table 3.3: Arrhenius parameters for the microkinetic reaction mechanism of ammonia decomposition and hydrogen oxidation over nickel catalyst, based on Appari *et al.* [19]

No.	**Reaction**	A **(cm, mol, s)**	β	E_a **(kJ mol^{-1})**
R1	$H_2 + 2\,(Ni) \longrightarrow 2\,H(Ni)$	1.0×10^{-2}	0	0.00
R2	$NH_3 + (Ni) \longrightarrow NH_3(Ni)$	1.1×10^{-2}	0	0.00
R3	$N_2 + 2\,(Ni) \longrightarrow 2\,N(Ni)$	1.0×10^{-6}	0	0.00
R4	$2\,H(Ni) \longrightarrow H_2 + 2\,(Ni)$	3.315×10^{19}	0	82.21
R5	$NH_3(Ni) \longrightarrow NH_3 + (Ni)$	8.210×10^{14}	0	78.63
R6	$2\,N(Ni) \longrightarrow N_2 + 2\,(Ni)$	4.442×10^{22}	0	210.84
R7	$NH_3(Ni) + (Ni) \longrightarrow NH_2(Ni) + H(Ni)$	5.723×10^{22}	0	78.99
R8	$NH_2(Ni) + H(Ni) \longrightarrow NH_3(Ni) + (Ni)$	1.320×10^{24}	0	48.81
R9	$NH_2(Ni) + (Ni) \longrightarrow NH(Ni) + H(Ni)$	2.718×10^{22}	0	75.74
R10	$NH(Ni) + H(Ni) \longrightarrow NH_2(Ni) + (Ni)$	3.702×10^{19}	0	74.87
R11	$NH(Ni) + (Ni) \longrightarrow N(Ni) + H(Ni)$	6.213×10^{19}	0	22.93
R12	$N(Ni) + H(Ni) \longrightarrow NH(Ni) + (Ni)$	2.070×10^{19}	0	156.04
R13	$O_2 + 2\,(Ni) \longrightarrow 2\,O(Ni)$	1.0×10^{-2}	0	0.00
R14	$O(Ni) + O(Ni) \longrightarrow O_2 + 2\,(Ni)$	3.928×10^{23}	0	473.41
R15	$H_2O + (Ni) \longrightarrow H_2O(Ni)$	1.0×10^{-1}	0	0.00
R16	$H_2O(Ni) \longrightarrow H_2O + (Ni)$	4.747×10^{12}	0	62.09
R17	$O(Ni) + H(Ni) \longrightarrow OH(Ni) + (Ni)$	5.000×10^{22}	0	97.90
R18	$OH(Ni) \longrightarrow O(Ni) + H(Ni)$	1.761×10^{20}	0	36.00
R19	$OH(Ni) + H(Ni) \longrightarrow H_2O(Ni) + (Ni)$	3.000×10^{20}	0	42.70
R20	$H_2O(Ni) + (Ni) \longrightarrow OH(Ni) + H(Ni)$	2.068×10^{21}	0	91.07
R21	$OH(Ni) + OH(Ni) \longrightarrow O(Ni) + H_2O(Ni)$	3.000×10^{21}	0	100.00
R22	$O(Ni) + H_2O(Ni) \longrightarrow OH(Ni) + OH(Ni)$	5.871×10^{23}	0	210.27

3.7 Pseudo one-dimensional PFR

From the currently available OpenFOAM implementations, catalyticFoam was chosen as the choice for modelling ammonia decomposition [32]. For comparison with the Cantera models, a pseudo 1-dimensional PFR was made in OpenFOAM. This validation was done for the mass fractions and the temperature profiles.

This model consisted of an inlet and outlet, as well as two catalytic walls, in a long and thin reactor. The remaining two walls were prescribed empty boundary conditions. Three uniform velocity profiles (0.005 m/s, 0.02 m/s and 0.05 m/s) were imposed along with no slip boundary conditions along the walls. The narrow inlet inhibits backward flow and radial mixing, which are assumptions in an ideal PFR.

The mesh was divided into 553 points along the streamwise direction, which was the

same as the number of points evaluated in Cantera. A catalytic ratio (catalyst area to total area) geometry ratio of 50 was assumed.

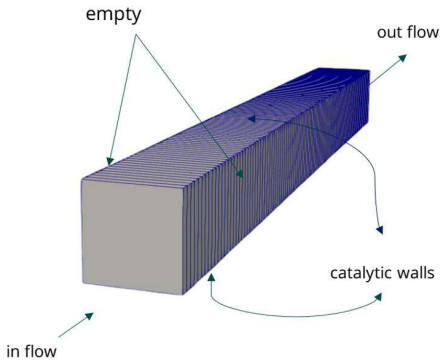

Figure 3.2: Pseudo PFR model in OpenFOAM.

Scheme Category	**Selected Scheme**
ddtSchemes	Euler
gradSchemes	Gauss upwind phi
divSchemes	Gauss upwind (e.g., div(phi,U)) Gauss limitedLinear01 1 (e.g., div(phi,Yi_h))
laplacianSchemes	Gauss linear orthogonal
interpolationSchemes	linear
snGradSchemes	orthogonal

Table 3.4: OpenFOAM fvSchemes for 1D PFR simulation

Parameter	Value
Dimension	0.1 m × 0.01 m × 0.01 m
Velocity	0.005 m/s , 0.02 m/s, 0.05 m/s
Temperature	1000 K
Pressure	101325 Pa
NH_3 (at inlet)	100%
H_2 (at inlet)	0%
N_2 (at inlet)	0%

Table 3.5: Parameters for 1D PFR simulation

3.8 2D axisymmetric setup

In order to model the decomposition of ammonia in a cylindrical reactor, a two-dimensional axisymmetric model was made in OpenFOAM similar to the one made by Robledo Asencio *et al.* [38]. Using the cylindrical symmetry of the reactor, this simulation can be performed in a 2D domain. This model was specifically tailored for the catalytic chamber and was implemented in this thesis. Figure 3.3 shows the boundary definition in the domain along with major dimensions.

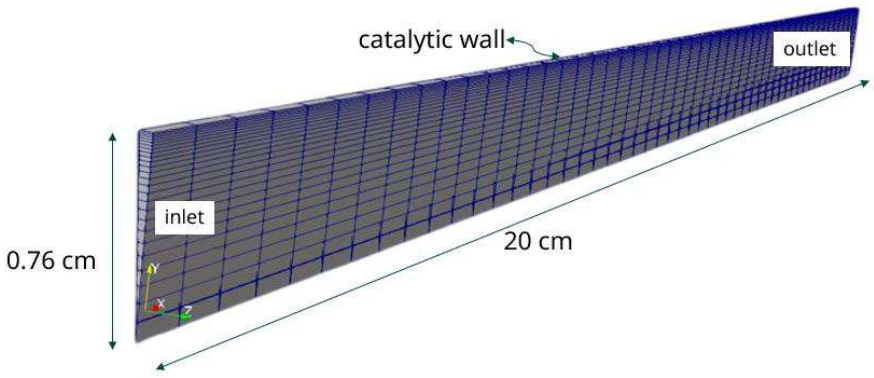

Figure 3.3: 2D axisymmetric setup

Spatial discretization consisted of 100 elements along the streamwise direction and 25 elements across the radial direction. Mesh grading was added in the radial direction

near the wall; Mesh grading is the process of adjusting the spatial distribution of mesh resolution—typically through systematic variation of cell size—in order to capture regions of high solution gradients (e.g., near walls, interfaces, or reaction zones) with greater precision, while maintaining coarser resolution in regions of relatively uniform behaviour. This grading ratio was set to be 10. The total number of cells in this domain was 1250.

As for the initial conditions, a pressure of 101325 Pa (1 atm) was imposed at the domain and for the initialised inlet gas feed. The gas feed mixture consisted of complete ammonia within the domain and at the inlet. A temperature of 800 K was imposed on the domain and inlet gas feed. A parabolic velocity, with a maximum value of 0.005 m/s, was defined because initialising a uniform bulk velocity led to unstable numerical outputs in the sampling likely due to sharp gradients in the entrance length of the domain. A catalytic area to geometry area ratio of 100 was defined. The Arrhenius parameters from the Zhang *et al.* [15] mechanism were defined as the kinetic scheme for the catalytic wall.

The data was sampled across the domain along the radial and streamwise directions. This included 25 radial lines equally spaced along the streamwise direction and 10 streamwise lines equally spaced along the radial direction.

Heterogeneous reactions were enabled while homogeneous reactions were disabled. This is realistic for ammonia decomposition in a catalytic reactor, where the reaction primarily occurs on the catalyst surface (e.g., on a ruthenium-based catalyst supported on yttria-stabilized zirconia, as noted in Zhang *et al.* [15]. Furthermore, ammonia decomposition involves adsorption, surface reactions and desorption steps. By focusing the surface reactions, the model would accurately represent the dominance of the heterogenous reactions [15].

Another essential component that predominantly differentiates the 2-D axisymmetric case from the 1-D PFR is the inclusion of accurate diffusion models. In a real reactor, the gas mixture consists of multiple species with distinct molecular properties. The mixture-averaged calculates mixture-averaged diffusion coefficients based on the approach proposed by Coffee and Heimerl [42]. This approach more accurately captures the diffusion dynamics in a multi-species system because of species specific diffusion coefficients,

as opposed to constant Lewis numbers. Further, Lewis numbers cannot capture preferential diffusion or differential diffusion effects, which may be important in understanding catalytic activity. F

The Soret effect accounts for thermal diffusion, where species migrate due to temperature gradients. In ammonia decomposition, the reaction is endothermic leading to temperature gradients near the catalyst surface as heat is absorbed. These gradients can drive lighter species like hydrogen towards cooler regions and heavier species like nitrogen towards hotter regions, influencing local concentrations and reaction rates. Additionally, enabling 'mass diffusion in energy equation' ensures that the energy transport equation accounts for enthalpy transport due to species diffusion, which is critical in a system with multiple species, where species-specific enthalpies vary significantly. This ensures that the thermal and mass transport phenomena are coupled accurately, mirroring the behaviour in a real reactor.

The operator-splitting approach used the Strang algorithm, a second-order accurate splitting method, which alternates between solving these subprocesses in a fractional step approach, typically performing half a transport step, a full reaction step, and the remaining half transport step within each time increment to maintain accuracy and stability [32]. This would decouple the transport, reaction, and momentum equations for numerical efficiency while maintaining accuracy. This is particularly suitable for catalytic systems where surface reactions (fast timescales) and fluid transport (slower timescales) occur at different rates. A relative and absolute tolerance of 1×10^{-7} and1×10^{-12} respectively would ensure accurate integration of the stiff differential equations arising from the microkinetic model. The simulation conditions and initial conditions are described in the following tables.

Table 3.6: Simulation conditions

Parameter	**Value**
Domain geometry	2D axisymmetric
Streamwise elements	100
Radial elements	25
Mesh grading ratio (radial)	10
Total cells	1250
Catalytic area to geometry area ratio	100
Diffusion model	Mixture-averaged [32]
Thermal diffusion (Soret effect)	Enabled
Mass diffusion in energy equation	Enabled
Reaction type	Heterogeneous only
Operator splitting method	Strang splitting (2nd-order)
Time integration tolerances	Rel: 1×10^{-7}, Abs: 1×10^{-12}

Table 3.7: Initial conditions

Parameter	**Value**
Pressure	101325 Pa (1 atm)
Temperature	800 K
Velocity profile	Parabolic
Maximum velocity	0.005 m/s
Initial species	100% NH_3 in the inlet and initial domain
Catalyst model	Ruthenium/Yttria-stabilized zirconia
Kinetic scheme	Zhang *et al.* [15]

4 Results and discussion

This section describes the results from Cantera and OpenFOAM simulations regarding ammonia decomposition over a catalyst using the Zhang *et al.* [15] mechanism for both the 1D plug flow reactor model and 2D axisymmetric. It mainly includes plots for mass fractions and temperatures, along with an analysis of how these parameters that change with the simulation.

4.1 Ammonia mass fraction variation over ruthenium and nickel catalyst (based on Zhang *et al.* [15] and Appari *et al.* [19], respectively)

In order to study which the catalytic effect of the mechanisms by Zhang *et al.* [15] and Appari *et al.* [19], the script described in 3 and attached in this appendix of the thesis, was used to obtain the amount of ammonia converted into nitrogen and hydrogen over a range of temperatures and velocities. Both, Fig. 4.1 and Fig. 4.2 were created with a pressure of 1 atmosphere and a catalytic area to volume ratio of 200 cm^{-1} to ammonia conversion.

The temperature range for the ruthenium catalyst was from 600 to 900 K, and it showed the temperature increase consistent with the results of Appari *et al.* [19].

A noteworthy difference between the two catalysts is the temperature threshold required for appreciable conversion. The ruthenium catalyst shows measurable activity at temperatures as low as 600 K, whereas the nickel catalyst requires temperatures above 700 K to achieve comparable conversion levels. This observation aligns with previous

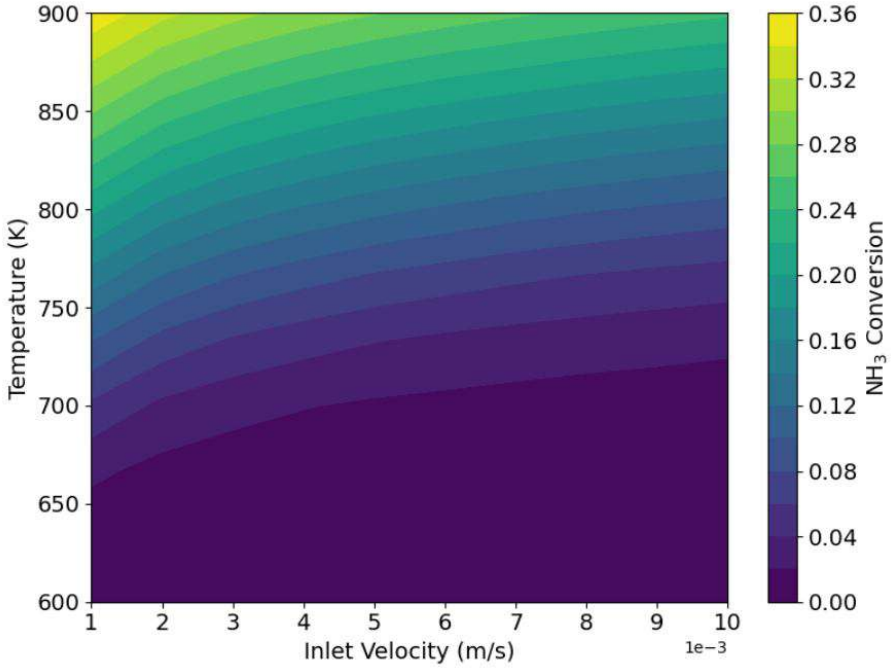

Figure 4.1: Ammonia mass fraction variation for velocity and temperature over ruthenium catalyst (based on the mechanism by Zhang *et al.* [15])

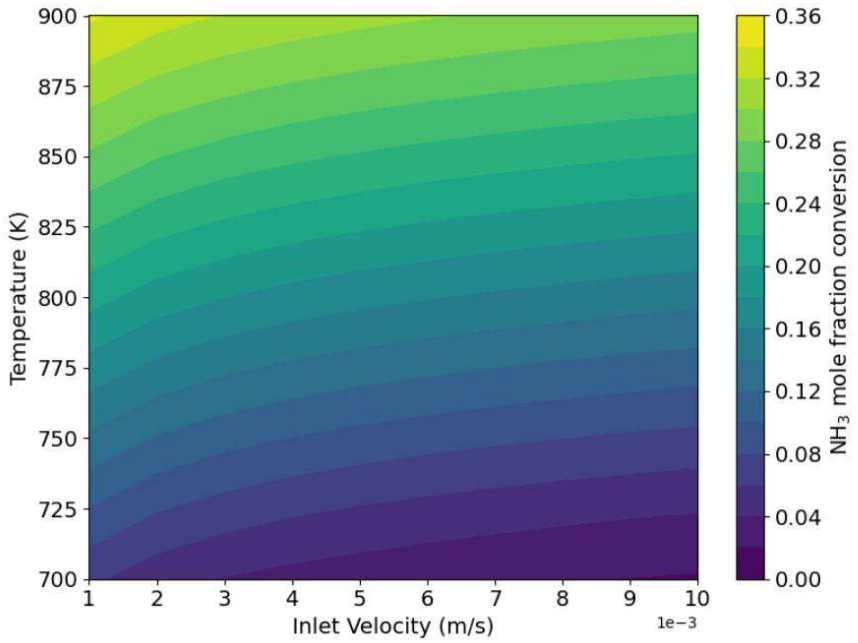

Figure 4.2: Ammonia mass fraction variation for velocity and temperature over nickel catalyst (based on the mechanism by Appari *et al.* [19])

studies that have consistently identified ruthenium as a more active catalyst for ammonia decomposition at lower temperatures compared to nickel, as mentioned in Su *et al.* [2].

The inlet velocity, which inversely correlates with residence time, also significantly impacts ammonia conversion for both catalysts. At all temperatures, decreasing the inlet velocity from 0.01 m/s to 0.001 m/s results in substantially higher NH_3 conversion. This relationship can be attributed to the increased residence time, and subsequently, the time the fluid is in contact with the catalytic surface between [43].

The subsequent simulations in this thesis are carried out using the mechanism by Zhang *et al.* [15] with catalyticFoam, since it was more recent in its publication.

4.2 One-dimensional plug flow reactor in Cantera and OpenFOAM

Using the Cantera code, a plot for the plug flow reactor was created and plotted against data from the OpenFOAM plug flow reactor. Wéry *et al.* [40] adopted a similar method by using catchyCFDEM to simulate a packed bed reactor and comparing the resulting mass fraction profiles with those from a one-dimensional plug flow simulation in Cantera.

The simulation conditions are described in table 3.5.

4.2.1 PFR results for velocity of $0.005\,\mathrm{m\,s^{-1}}$

Table 4.1: Average relative difference between Cantera and OpenFOAM results for species mass fractions and temperature (0.005 m/s).

Quantity	**Average difference (%)**
NH_3 mass fraction	4.67
H_2 mass fraction	31.47
N_2 mass fraction	30.38
Temperature (K)	4.74

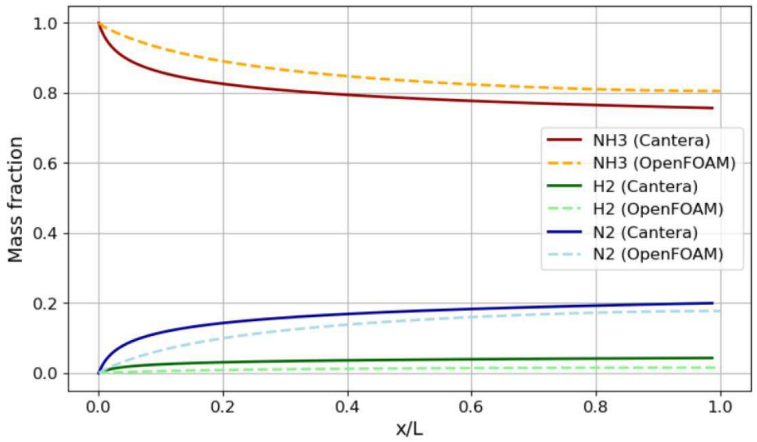

Figure 4.3: Mass fraction of species in OpenFOAM and Cantera (velocity = 0.005 m/s)

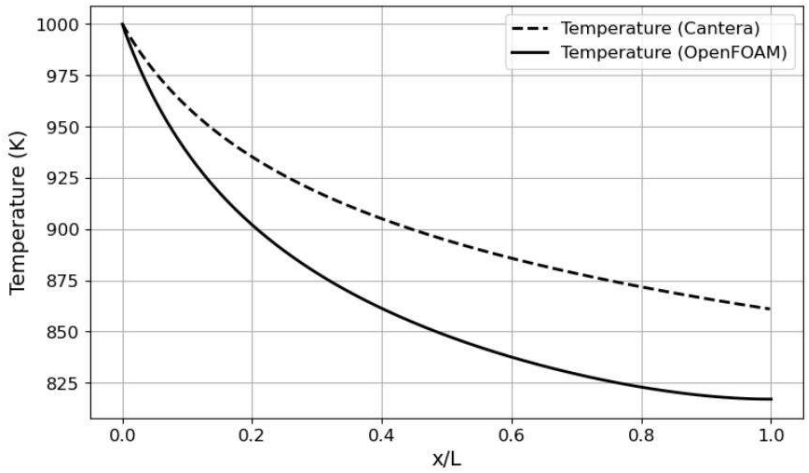

Figure 4.4: Temperature profile in OpenFOAM and Cantera (velocity = 0.005 m/s)

Figure 4.3 shows the species mass fraction variation along the length of the reactor. This reactor length is normalized by dividing it with the total length for easier interpretation of results. As can be observed, the mass fractions from Cantera and OpenFOAM follows a relatively constant discrepancy with no noticeable 'overlap'. The temperature profile, plotted in Figure 4.4 shows a discrepency that increases along the length of the reactor between the Cantera and OpenFOAM results.

4.2.2 PFR results for velocity of $0.02\,\mathrm{m\,s^{-1}}$

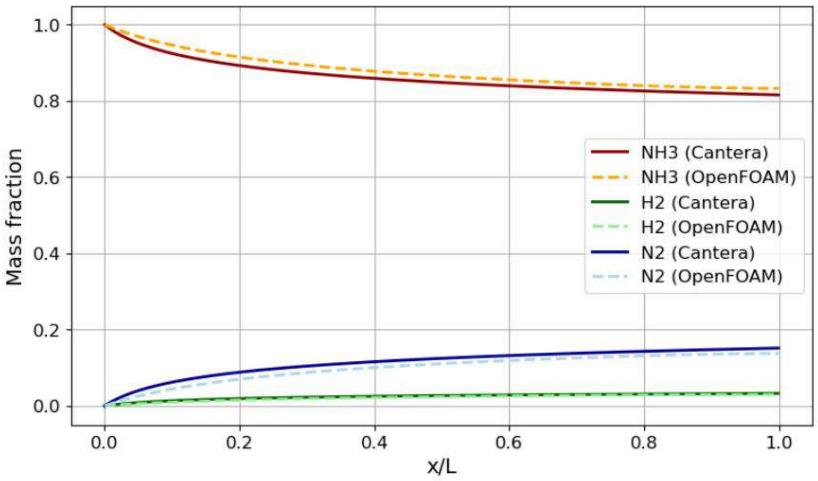

Figure 4.5: Mass fraction of species in OpenFOAM and Cantera (velocity = 0.02 m/s)

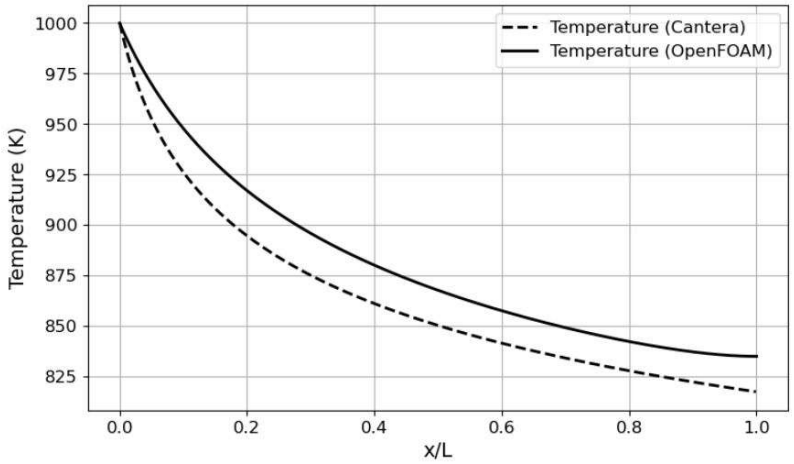

Figure 4.6: Temperature in OpenFOAM and Cantera (velocity = 0.02 m/s)

Table 4.2: Average relative difference between Cantera and OpenFOAM results for species mass fractions and temperature (0.02 m/s).

Quantity	**Average difference (%)**
NH_3 mass fraction	1.95
H_2 mass fraction	19.4
N_2 mass fraction	19.5
Temperature (K)	1.98

When the velocity is increased from $0.005\,\mathrm{m\,s^{-1}}$ to $0.02\,\mathrm{m\,s^{-1}}$, the discrepancy between the mass fractions noticeably reduces (as seen in figure 4.5). A similar reduction in the difference is seen in the temperature profile as well.

4.2.3 PFR results for velocity of $0.05\,\mathrm{m\,s^{-1}}$

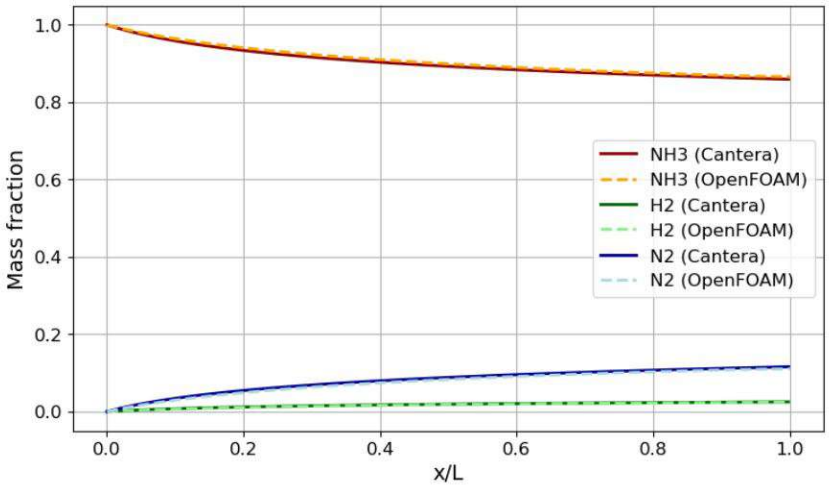

Figure 4.7: Mass fraction of species in OpenFOAM and Cantera (velocity = 0.05 m/s)

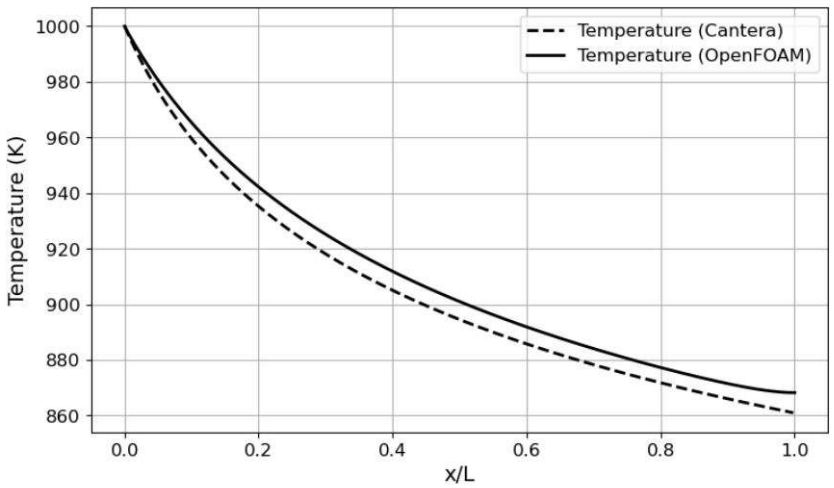

Figure 4.8: Temperature in OpenFOAM and Cantera (velocity = 0.05 m/s)

Table 4.3: Average relative difference between Cantera and OpenFOAM results for species mass fractions and temperature (0.05 m/s).

Quantity	**Average difference (%)**
NH_3 mass fraction	0.64
H_2 mass fraction	8.99
N_2 mass fraction	8.99
Temperature (K)	0.66

Similar to the previous two cases, When the velocity is increased to $0.05\,\mathrm{m\,s^{-1}}$, the discrepancy between the mass fractions and temperature, once again, reduces (as seen in figures 4.7 and 4.8 respectively).

4.3 Discussion on 1D PFR results

As velocity is increased, the residence time of reactants in the reactor decreases proportionally. With shorter residence times at higher velocities, ammonia has less time to interact with the catalyst and complete the reaction. This is evident in the lower final NH_3 mass fractions and higher product (H_2 and N_2) mass fractions at lower velocities.

As far as the differences between the OpenFOAM and Cantera results are concerned,

increasing the velocity reduces the difference between them. This is because the cumulative effect of the differences in modelling between OpenFOAM and Cantera is reduced. Further, at lower velocities, boundary layer effects are more pronounced, and the pseudo-1D approach in OpenFOAM may not capture these effects as accurately as Cantera's 1D solver.

Additionally, the Péclet number ($\mathrm{Pe} = \frac{UL}{D}$) increases with velocity, reducing the relative importance of diffusion compared to convection. At higher velocities, convection dominates the transport process, making both models more similar.

Moreover, diffusivity was suppressed by increasing Lewis numbers in the OpenFOAM simulations and the artificial suppression becomes more effective at higher velocities where convective transport already dominates, further reducing discrepancies between the models.

4.4 2D axisymmetric results

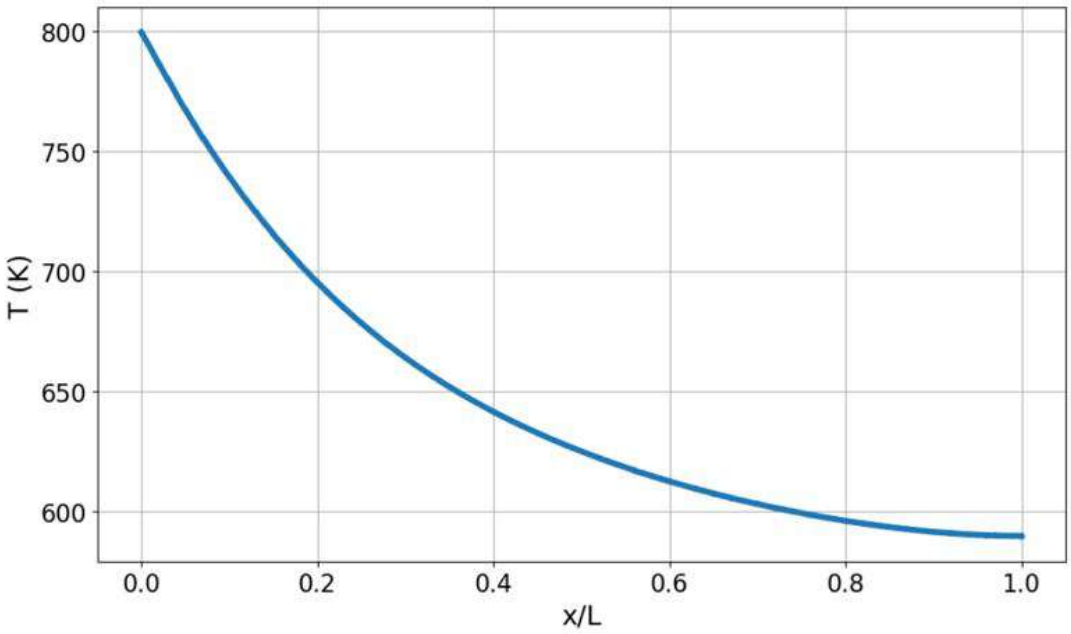

Figure 4.9: Average temperature profile in streamwise direction.

Figure 4.9 shows an exponential decrease in gas temperature from approximately 800

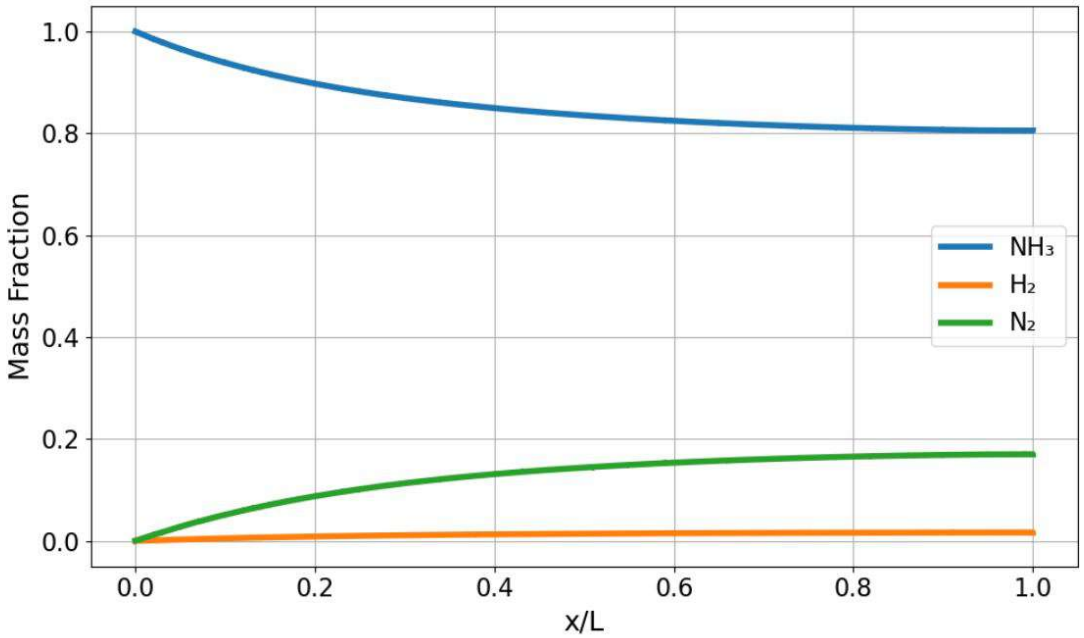

Figure 4.10: Average mass fractions in streamwise direction.

K at the inlet ($x/L = 0$) to less than 600 K at the outlet ($x/L = 1.0$). Simultaneously, the mass fractions of ammonia decrease along the reactor, resulting in a commensurate increase of nitrogen and hydrogen, as seen in Figure 4.10. This represents the endothermic nature of the reaction.

This significant energy requirement directly influences the temperature profile observed in the reactor. As ammonia decomposes, it draws heat from the surrounding gas mixture, leading to a decrease in temperature along the reactor length. In an adiabatic reactor, where no heat is exchanged with the surroundings, this temperature drop would be solely due to the energy consumed by the reaction. In a non-adiabatic reactor, heat transfer to or from the surroundings would also play a role. However, the observed temperature decrease strongly indicates that the endothermic reaction is the dominant factor governing the thermal behaviour of the system.

To further understand the energy balance within the reactor, the absolute enthalpy of the mixture at both the inlet and outlet was calculated. At the inlet, with 100% ammonia at 800 K, the enthalpy was approximately -1412.47 kJ/kg. The wall was assumed non-adiabatic and a no-slip boundary condition was applied. At the outlet, with the given

mass fractions of approximately 0.8 NH_3, 0.02 H_2, and 0.18 N_2 at 590 K, the enthalpy was approximately -1367.76 kJ/kg. The change in enthalpy from inlet to outlet is approximately $+44.71$ kJ/kg, closely corresponding to the standard enthalpy change in Equation (2.2). This positive change in enthalpy of the flowing mixture indicates that the system has absorbed energy, which is consistent with an endothermic reaction consuming heat as it progresses and leading to a temperature drop.

4.4.1 Velocity field

At the inlet of the 2D axisymmetric reactor, a parabolic velocity profile is imposed with a maximum velocity of 0.005 m/s. This is characteristic of fully developed laminar flow in a cylindrical pipe. For laminar flow, the fluid moves in layers, and due to the no-slip boundary condition at the reactor walls (where velocity is zero), the velocity increases towards the centre of the pipe, reaching a maximum at the centreline.

This behaviour is governed by the Navier–Stokes equations for incompressible, steady, laminar flow in a pipe, using the Hagen–Poiseuille equation.

The velocity distribution across the pipe radius is given by the parabolic profile:

$$u(r) = u_{\max}\left(1 - \left(\frac{r}{R}\right)^2\right)$$

where $u(r)$ is the axial velocity at radial position r, $u_{\max}$ is the maximum velocity at the centreline, and R is the pipe radius.

While a decrease in viscosity, in isolation, would typically lead to an increase in fluid velocity for a given pressure gradient, the observed decrease in centreline velocity suggests that other factors are at play, with density being a primary candidate. As per the ideal gas law, the large decrease in temperature would lead to a decrease in density, which would lead to a viscosity change. Taking exact values from the centreline at the inlet and outlet along the streamwise direction, before the reaction, the gas mixture consists solely of ammonia, with a molar mass of 17.03 g/mol. After decomposition of 20% of the ammonia, the resulting mixture would have an average molar mass of 14.19 g/mol. This decrease in average molecular weight tends to decrease the density. Coupled with

the temperature drop, this leads to two opposing effects that influence density: the decreasing temperature tends to increase density, while the decreasing average molecular weight tends to decrease density (as per the ideal gas law).

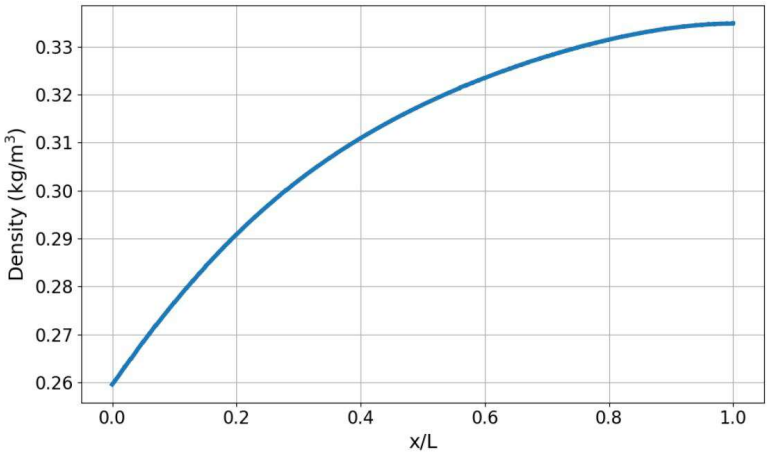

Figure 4.11: Density variation along streamwise direction.

This increase in density, for a constant mass flow rate, would lead to a decrease in velocity, which is observed from the figures below.

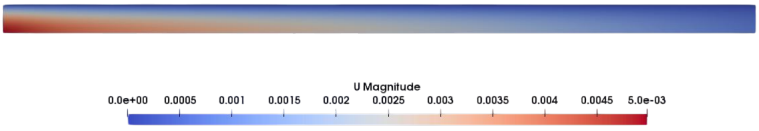

Figure 4.12: Velocity contours at t = 10 s.

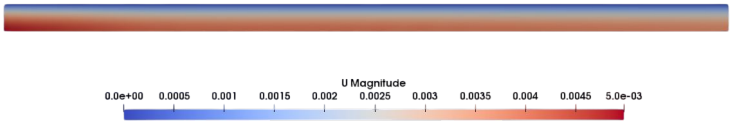

Figure 4.13: Velocity contours at t = 60 s.

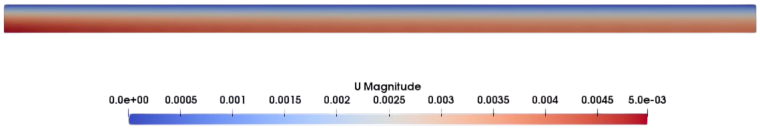

Figure 4.14: Velocity contours at t = 100 s.

As can be seen, the velocity profile near the inlet follows the parabolic profile, but as the reaction proceeds along the streamwise direction, the combining effects of the density and viscosity increase reduce the'maxima' of the velocity to around 0.004 m/s.

4.4.2 Impact of mixture-averaged diffusion on temperature and mass fraction profiles

In reacting or non-reacting gas mixtures, the mixture-averaged diffusion model describes the transport of individual species due to molecular diffusion resulting from concentration gradients and temperature gradients [32].

The mixture-averaged model is particularly important in high-fidelity simulations of chemically reacting flows, such as combustion, catalytic reactions, or high-temperature gas-phase processes, where the assumption of independent diffusion, using unity Lewis numbers for instance, fails to capture the true transport dynamics.

In a system with multiple species, the driving force for the diffusion of a particular species is the gradient of its chemical potential, which is closely related to its concentration gradient. However, the diffusion flux of a given species is not solely determined by its own concentration gradient; it also depends on the gradients of other species in the mixture and on the intermolecular friction between different molecular pairs. As a result, the transport of a reactant toward a catalytic surface may be either hindered or enhanced by the counter-diffusion of reaction products or the presence of inert species [44].

Observing the data for the mass fractions of all species as well as the temperature, it seems that these quantities remain very much close with each other, near the catalytic wall and near the centerline, as summarized in the table below:

Table 4.4: Comparison of gas properties near centreline and near catalytic wall

Property	**Near centreline**	**Near catalytic wall**
Temperature (K)	590.04	589.94
NH_3 Mass fraction	0.80518	0.80507
H_2 Mass fraction	0.016425	0.016430
N_2 Mass fraction	0.16986	0.16995

The data from this table gives some insights. Firstly, the production of hydrogen

and nitrogen near the catalytic wall is faster than the diffusion that occurs, leading to a relatively constant mass fraction for both these mass fractions. Since the domain is initialised entirely with ammonia, the amount of ammonia is slightly lower than near the centreline because of its decomposition being highest near the catalytic wall.

Furthermore, as the gas mixture moves along the reactor and cools, the molecular diffusion coefficients of all species will decrease. This reduction in diffusivity means that the rate at which NH_3, H_2 and N_2 can diffuse to the catalyst surface, will slow down in the downstream sections of the reactor. This effect can exacerbate diffusion limitations, making them more pronounced in the cooler regions, even if the concentration gradients remain similar.

The presence of diffusion limitations influences the catalytic activity in a reactor. When the mass transfer rate of the reactants to the catalyst surface is slower than the intrinsic chemical reaction rate, the catalyst is unable to perform at its theoretical maximum efficiency. Consequently, the observed reaction rate becomes limited not by the catalyst's kinetics but by the rate at which reactants can reach active sites.

One of the primary consequences of diffusion limitations is a reduced apparent reaction rate [45]. In the context of ammonia decomposition, a local depletion of ammonia at the catalyst surface reduces the concentration gradient that drives the reaction. Even in cases where the catalyst has high intrinsic activity, this resistance to mass transfer reduces its effectiveness [44].

This reduction in surface concentration and reaction rate leads to a *lower overall conversion* of ammonia to nitrogen and hydrogen. The effect becomes particularly pronounced in downstream regions of the reactor, where lower temperatures further hinder diffusion rates.

Although ammonia decomposition involves a single reaction pathway, in more complex systems involving parallel or consecutive reactions, diffusion limitations can also influence *reaction selectivity*. Reactions that are less diffusion-limited may become preferential, potentially altering the desired product distribution [46]. Although this aspect is not directly relevant to the present system, it remains a critical consideration in general

catalytic reactor design.

Finally, for endothermic reactions such as ammonia decomposition, diffusion limitations can contribute to adverse *temperature effects*. Limited diffusion of ammonia to the catalyst surface results in slower reaction rates, leading to reduced heat absorption. This creates a feedback loop of falling temperature and decreasing intrinsic reaction rates, which ultimately decreases the performance of the reactor [44], [47].

4.5 Averaged radial profiles across streamwise direction

The plot below shows the average of the mass fractions along the streamwise directions, compared with an equivalent 1D plug flow reactor model.

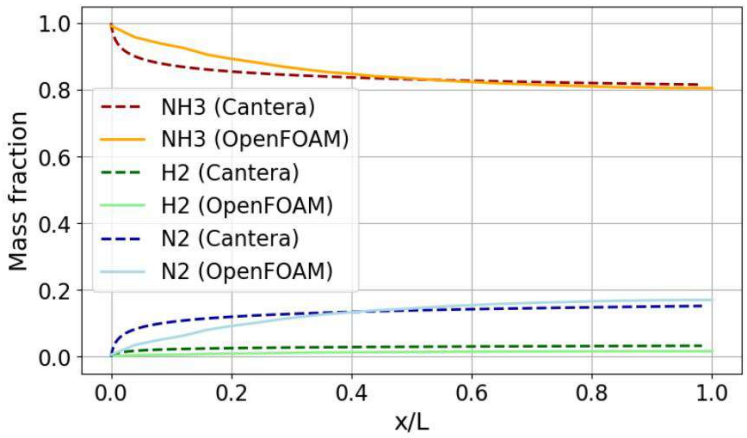

Figure 4.15: Mass fraction averages along streamwise directions compared with equivalent 1D PFR

It can be observed that during the first 30 % of the reactor length, the Cantera PFR seems to overpredict the ammonia conversion before coming in line with the OpenFOAM 2D results.

The discrepancies observed between the radially averaged 2D axisymmetric OpenFOAM simulations and the 1D Cantera plug flow reactor (PFR) model stem from fundamental differences in their treatment of transport phenomena and reactor geometry.

The Cantera PFR model assumes ideal plug flow, characterised by uniform veloc-

ity and negligible radial gradients, implying that all fluid elements experience identical residence times and follow a single-path reaction progression. In contrast, the 2D OpenFOAM simulation captures radial velocity gradients, such as the parabolic profile typical of laminar flow, where faster-moving fluid at the centre has shorter residence times, while slower near-wall fluid undergoes prolonged reaction. This radial variation, when averaged, results in lower NH_3 conversion, manifesting as a flatter decay curve compared to the PFR model, and reduced H_2/N_2 yields near the outlet due to incomplete reactions in the high-velocity core.

Furthermore, the PFR model neglects molecular diffusion, assuming instantaneous radial mixing and concentration dependence solely on axial position. The OpenFOAM simulation, however, resolves finite-rate radial diffusion, leading concentration gradients (albeit small) between the centreline and wall, slower NH_3 consumption in regions where diffusion lags behind reaction (e.g., the high-velocity core), and delayed H_2/N_2 formation relative to PFR predictions, particularly at intermediate axial positions ($0.3 < x/L < 0.7$).

Additionally, the PFR model overlooks wall interactions, such as heat transfer or catalytic/non-catalytic boundaries, whereas OpenFOAM accounts for catalytic wall reactions, which accelerate NH_3 decomposition near walls, and heat transfer to walls, potentially quenching reactions in boundary layers. These wall effects contribute to local deviations, such as a steeper NH_3 drop near walls but a flatter centreline profile.

These differences highlight the limitations of the 1D PFR model in capturing the complex interplay of transport and reaction phenomena in real reactor systems.

5 Conclusion

5.1 Summary

Ammonia is a promising hydrogen vector that can have a critical role in clean energy applications. This thesis was incentivised for this reason, and it investigated the ammonia decomposition reaction through CFD simulations. Using a published reaction mechanism by Zhang *et al.* [15] and a solver created by Maestri and Cuoci [32] called catalyticFoam, these simulations examined how temperatures and mass fraction of species varied along the reactor and how the complex interplay of parameters can be influential. The endothermic ammonia decomposition reaction is thermodynamically favoured, only at high temperatures, and proceeds at negligible rates without a suitable catalyst. Thus, catalytic ammonia cracking is essential for practical hydrogen generation, and the work began by reviewing and selecting appropriate kinetic models and catalysts.

Kinetic mechanisms range from simple empirical power-law rates to detailed microkinetic mechanisms, each with variations in complexity and accuracy. However, the two most compatible mechanisms, in the context of utilization with OpenFOAM, were published by Appari *et al.* [19] for nickel and Zhang *et al.* [15]. Following an initial plug-flow reactor modelling using Cantera for both the mechanisms, the Zhang *et al.* [15] mechanism was chosen for subsequent simulations with OpenFOAM.

Two modelling approaches were employed to simulate the ammonia cracker, accounting for complexity. First, a pseudo one dimensional (1D) plug-flow reactor (PFR) model was implemented in OpenFOAM, the 1D model assuming complete mixing in the radial direction (as seen in an ideal PFR) and sets to simulate the axial conversion under more

simple conditions. It was used to validate reaction kinetics and to rapidly explore parameter effects. The OpenFOAM 1D results were cross-validated against a Cantera plug-flow simulation under identical conditions, assuring that the kinetics and thermo-physical data were correctly implemented. The Cantera and OpenFOAM PFR profiles were found to be in a precise overall agreement, and a similar approach has been concluded in the literature (for instance, Wéry *et al.* [40] used a coupled OpenFOAM–Cantera method for packed bed reactors).

Secondly, a two-dimensional axisymmetric CFD model of a tubular catalytic reactor was developed. This 2D model represents a cylindrical flow channel with a catalytic wall, thus capturing radial gradients of velocity, species, and temperature. It employs the full set of governing equations (the conservation of mass, momentum, energy, and species) with detailed transport models. Particularly, mixture-averaged diffusion model was equipped in the 2D simulation. Comparing the simplified 1D results against the more detailed 2D predictions allowed the study to identify which phenomena were neglected in the 1D model, and how they impacted reactor performance.

For the 1D PFR model, the OpenFOAM mass fractions and temperature profiles along the reactor were in closer agreement with their equivalent Cantera simulations as the velocity was increased. This trend indicates that the simplified 1D model is the most reliable under conditions where convective transport dominates and gradients are less pronounced. In fact, at higher velocities (higher Reynolds/Péclet numbers), convection overwhelms diffusion, making the plug-flow assumption more valid and reducing the model-to-model differences. The 1D model's fidelity at high flow rates is further improved by the numerical treatment: in the OpenFOAM PFR, an artificially high species Lewis number was used (where needed) to suppress excessive diffusion, mimicking the plug-flow behaviour. Generally, both of the 1D simulations demonstrated that the chosen kinetics can predict ammonia conversion within reasonable accuracy.

In the 2D reactor, ammonia is consumed on the catalytic wall surface, which creates radial concentration gradients – NH_3 is depleted near the wall while persisting longer along the centreline. Fluid near the centre flows more quickly and has a shorter residence

time due to the laminar flow, while fluid near the wall moves more slowly and reacts more thoroughly. This results in a flatter axial NH_3 profile (lower overall conversion at a given length) in the 2D simulation when averaged over the cross-section, as opposed to the optimal PFR prediction. In other words, the ideal 1D PFR tends to overestimate conversion because it assumes instantaneous radial mixing; the 2D model shows that some ammonia in the high-velocity core effectively bypasses the catalyst, thus emerging unreacted. This effect was observed in the CFD results as a more gradual NH_3 decay curve and correspondingly lower H_2 /N_2 yields towards the reactor outlet relative to the 1D model. The difference between the rate at which reactants reach the catalytic surface and the rate of reaction serves as an example of a common diffusion discrepancy. In the 1D model, diffusion is assumed to be infinite, so it cannot capture the mass transfer resistance effect. Additionally, the 1D PFR neglects any wall heat transfer or radial thermal gradients; conversely, the 2D simulation accounts for conduction of heat to the walls and the spatial distribution of reaction heat absorption. In the study, the reactor was effectively adiabatic with respect to the surroundings (no external heating along the length), so the dominant thermal effect was the reaction's endothermic cooling of the gaseous mixture. The 2D results showed how the reaction consumed energy, as a significant temperature drop along the flow was observed: from about 800 K at the inlet down to 600 K at the outlet. This can contribute to both the diffusion process of the individual species and to the rate of reaction as well.

As for the diffusion model, the impact of species diffusion on total ammonia conversion was modest, as bulk parameters such as temperature and flow residence time remained the dominant factors. However, while these transport effects may not significantly shift integral performance metrics under all conditions, they are essential for accurately capturing the local physics that govern reaction progression and heat transfer.

5.2 Future works

The simulations presented in this thesis work explore 1D and 2D simulations. However, for more realistic results, 3D simulations concerning pipe flows and capturing turbulence-based effects can offer more valuable insights in terms of efficient hydrogen production. While the catalyticFoam solver by Maestri and Cuoci [32] did not have LES (Large Eddy Simulations) or RANS (Reynolds Averaged Navier-Stokes) based modelling implemented in their source code for solving turbulence cases using OpenFOAM, high-fidelity DNS simulations are possible and can be used to study how the reaction rate is affected with small eddy flows or how the endothermic reactions may affect turbulence.

In addition to this, it is important to validate the CFD model with accurate experimental data, and draw comparisons with the experimental data, as done in Appari *et al.* [19], for instance. This would significantly increase the reliability of the model in using different reaction conditions or catalysts. Experimental validation can also give a stronger idea on the sensitivity of assumptions and can reveal significant model deficiencies, which can then be a basis to iteratively fix any underlying issues and have better and more accurate results.

References

[1] R. Ao, R. Lu, G. Leng, Y. Zhu, F. Yan, and Q. Yu, "A review on numerical simulation of hydrogen production from ammonia decomposition", *Energies*, vol. 16, no. 2, p. 921, 2023. DOI: 10.3390/en16020921. [Online]. Available: https://doi.org/10.3390/en16020921.

[2] T. Su *et al.*, "Review on ru-based and ni-based catalysts for ammonia decomposition: Research status, reaction mechanism, and perspectives", *Energy & Fuels*, vol. 37, no. 12, pp. 8099–8127, 2023. DOI: 10.1021/acs.energyfuels.3c00804.

[3] O. A. Ojelade and S. F. Zaman, "Ammonia decomposition for hydrogen production: A thermodynamic study", *Chemical Papers*, vol. 75, no. 1, pp. 57–65, 2021. DOI: 10.1007/s11696-020-01278-z.

[4] Ž. Ponikvar *et al.*, "Electrified dynamically responsive ammonia decomposition to hydrogen based on magnetic heating of a ru nanocatalyst", *ChemSusChem*, vol. 18, no. 8, e202401970, Apr. 2025. DOI: 10.1002/cssc.202401970.

[5] X. Huang, K. Lei, Y. Mi, W. Fang, and X. Li, "Recent progress on hydrogen production from ammonia decomposition: Technical roadmap and catalytic mechanism", *Molecules*, vol. 28, no. 13, Jan. 2023. DOI: 10.3390/molecules28135245.

[6] P. Shafie, A. DeChamplain, and J. Lepine, "Theoretical investigation of hydrogen-rich fuel production through ammonia decomposition", *Open Chem.*, vol. 22, pp. 1–9, 2024. DOI: 10.1515/chem-2024-0020.

[7] Y. Im, H. Muroyama, T. Matsui, K. Eguchi, Y. Kim, and H. Chae, "Multifunctional effect of copper in bimetallic cu-m/al2o3 catalysts (m = fe, co, and ni) for nh3

decomposition", *Applied Surface Science*, vol. 669, p. 160 396, Oct. 2024. DOI: 10.1016/j.apsusc.2024.160396.

[8] N. Itoh, A. Oshima, E. Suga, and T. Sato, "Kinetic enhancement of ammonia decomposition as a chemical hydrogen carrier in palladium membrane reactor", *Catalysis Today*, vol. 236, pp. 70–76, Nov. 2014. DOI: 10.1016/j.cattod.2014.02.054.

[9] S. Armenise, E. García-Bordejé, J. L. Valverde, E. Romeo, and A. Monzón, "A langmuir–hinshelwood approach to the kinetic modelling of catalytic ammonia decomposition in an integral reactor", *Phys. Chem. Chem. Phys.*, vol. 15, no. 29, pp. 12 104–12 117, Jul. 2013. DOI: 10.1039/C3CP50715G.

[10] I. Lucentini, G. G. Colli, C. D. Luzi, I. Serrano, O. M. Martínez, and J. Llorca, "Catalytic ammonia decomposition over ni-ru supported on ceo2 for hydrogen production: Effect of metal loading and kinetic analysis", *Applied Catalysis B: Environmental*, vol. 286, p. 119 896, Jun. 2021. DOI: 10.1016/j.apcatb.2021.119896.

[11] P. Yuan, L. Chen, C. Liu, and Z. Wang, "Numerical studies on hydrogen production from ammonia thermal cracking with catalysts", *Energies*, vol. 16, no. 13, Jan. 2023. DOI: 10.3390/en16135196.

[12] S. R. Kulkarni *et al.*, "Elucidating the rate-determining step of ammonia decomposition on ru-based catalysts using ab initio-grounded microkinetic modeling", *Catal. Sci. Technol.*, vol. 13, no. 7, pp. 2026–2037, Apr. 2023. DOI: 10.1039/D3CY00055A.

[13] H. Fang *et al.*, "Challenges and opportunities of ru-based catalysts toward the synthesis and utilization of ammonia", *ACS Catal.*, vol. 12, no. 7, pp. 3938–3954, Apr. 2022. DOI: 10.1021/acscatal.2c00090.

[14] Z. Su *et al.*, "Research progress of ruthenium-based catalysts for hydrogen production from ammonia decomposition", *International Journal of Hydrogen Energy*, vol. 51, pp. 1019–1043, Jan. 2024. DOI: 10.1016/j.ijhydene.2023.09.107.

[15] Z. Zhang, C. Karakaya, R. J. Kee, J. D. Way, and C. A. Wolden, "Barium-promoted ruthenium catalysts on yttria-stabilized zirconia supports for ammonia synthesis", *ACS Sustainable Chem. Eng.*, vol. 7, no. 21, pp. 18 038–18 047, Nov. 2019. DOI: 10.1021/acssuschemeng.9b04929.

[16] O. Hinrichsen, F. Rosowski, M. Muhler, and G. Ertl, "The microkinetics of ammonia synthesis catalyzed by cesium-promoted supported ruthenium", *Chemical Engineering Science*, Chemical Reaction Engineering: From Fundamentals to Commercial Plants and Products, vol. 51, no. 10, pp. 1683–1690, May 1996, ISSN: 0009-2509. DOI: 10.1016/0009-2509(96)00027-9. [Online]. Available: https://www.sciencedirect.com/science/article/pii/0009250996000279 (visited on 05/19/2025).

[17] A. S. Farooqi *et al.*, "A comprehensive review on hydrogen production via catalytic ammonia decomposition over ni-based catalysts", *International Journal of Hydrogen Energy*, vol. 97, pp. 593–613, Jan. 2025. DOI: 10.1016/j.ijhydene.2024.11.357.

[18] A. Takahashi and T. Fujitani, "Kinetic analysis of decomposition of ammonia over nickel and ruthenium catalysts", *Journal of Chemical Engineering of Japan*, vol. 49, no. 1, pp. 22–28, 2016. DOI: 10.1252/jcej.14we431.

[19] S. Appari, V. M. Janardhanan, S. Jayanti, L. Maier, S. Tischer, and O. Deutschmann, "Micro-kinetic modeling of nh3 decomposition on ni and its application to solid oxide fuel cells", *Chemical Engineering Science*, vol. 66, no. 21, pp. 5184–5191, Nov. 2011. DOI: 10.1016/j.ces.2011.07.007.

[20] Z. Lendzion-Bielun, U. Narkiewicz, and W. Arabczyk, "Cobalt-based catalysts for ammonia decomposition", *Materials*, vol. 6, no. 6, Jun. 2013. DOI: 10.3390/ma6062400.

[21] Z. Almisbaa and P. Sautet, "Ba promoter effect on cobalt-catalyzed ammonia decomposition kinetics: A theoretical analysis", *Journal of Energy Chemistry*, vol. 99, pp. 182–192, Dec. 2024. DOI: 10.1016/j.jechem.2024.07.050.

[22] A. Gunnarson, A. Cao, O. F. Sloth, *et al.*, "Theory-guided development of a barium-doped cobalt catalyst for ammonia decomposition", en, *Energy & Environmental Science*, vol. 17, no. 23, pp. 9313–9322, 2024, ISSN: 1754-5692, 1754-5706. DOI: 10.1039/D4EE02874K. [Online]. Available: https://xlink.rsc.org/?DOI=D4EE02874K (visited on 01/23/2025).

[23] S. C. Yeo, S. S. Han, and H. M. Lee, "Mechanistic investigation of the catalytic decomposition of ammonia (nh3) on an fe(100) surface: A dft study", *J. Phys. Chem. C*, vol. 118, no. 10, pp. 5309–5316, Mar. 2014. DOI: 10.1021/jp410947d.

[24] G. Lanzani and K. Laasonen, "Nh3 adsorption and dissociation on a nanosized iron cluster", *International Journal of Hydrogen Energy*, vol. 35, no. 13, pp. 6571–6577, Jul. 2010. DOI: 10.1016/j.ijhydene.2010.03.142.

[25] W. Arabczyk and J. Zamłynny, "Study of the ammonia decomposition over iron catalysts", *Catalysis Letters*, vol. 60, no. 3, pp. 167–171, Jul. 1999. DOI: 10.1023/A:1019007024041.

[26] J. W. Makepeace, T. J. Wood, H. M. A. Hunter, M. O. Jones, and W. I. F. David, "Ammonia decomposition catalysis using non-stoichiometric lithium", *Chem Sci*, vol. 6, no. 7, pp. 3805–3815, Jul. 2015. DOI: 10.1039/c5sc00205b.

[27] J. W. Makepeace, H. M. A. Hunter, T. J. Wood, R. I. Smith, C. A. Murray, and W. I. F. David, "Ammonia decomposition catalysis using lithium–calcium imide", *Faraday Discuss.*, vol. 188, pp. 525–544, 2016. DOI: 10.1039/C5FD00179J.

[28] T. J. Wood, J. W. Makepeace, H. M. A. Hunter, M. O. Jones, and W. I. F. David, "Isotopic studies of the ammonia decomposition reaction mediated by sodium amide", *Phys. Chem. Chem. Phys.*, vol. 17, no. 35, pp. 22 999–23 006, Aug. 2015. DOI: 10.1039/C5CP03560K.

[29] W. Bizon, "Modelling of ammonia decomposition in a fixed bed reactor with ruthenium catalyst", *Energies*, vol. 14, no. 1, p. 208, 2021. DOI: 10.3390/en14010208. [Online]. Available: https://www.mdpi.com/1996-1073/14/1/208.

[30] G. D. Wehinger, N. Jurtz, and M. Kraume, "Multiscale simulation of fixed-bed catalytic reactors: A review of models and applications", *Energies*, vol. 14, no. 1, p. 208, 2021. DOI: 10.3390/en14010208. [Online]. Available: https://www.mdpi.com/1996-1073/14/1/208.

[31] N. Jurtz, U. Srivastava, A. A. Moghaddam, and M. Kraume, "Particle-resolved computational fluid dynamics as the basis for thermal process intensification of fixed-bed reactors on multiple scales", *Energies*, vol. 14, no. 10, p. 2913, 2021. DOI: 10.3390/en14102913. [Online]. Available: https://www.mdpi.com/1996-1073/14/10/2913.

[32] M. Maestri and A. Cuoci, "Coupling cfd with detailed microkinetic modeling in heterogeneous catalysis", *Chemical Engineering Science*, vol. 96, pp. 106–117, 2013. DOI: 10.1016/j.ces.2013.03.048. [Online]. Available: http://www.catalyticfoam.polimi.it/.

[33] D. G. Goodwin, H. K. Moffat, I. Schoegl, R. L. Speth, and B. W. Weber, *Cantera: An object-oriented software toolkit for chemical kinetics, thermodynamics, and transport processes*, https://www.cantera.org, Version 3.1.0, 2024. DOI: 10.5281/zenodo.14455267.

[34] Cantera Developers, *Plug flow reactor — cantera documentation*, Accessed: 2025-05-27, Cantera Project, 2025. [Online]. Available: https://cantera.org/dev/reference/reactors/pfr.html.

[35] Wikipedia contributors, *File:pipe-pfr.svg — wikipedia, the free encyclopedia*, Accessed: May 28, 2025, 2024. [Online]. Available: https://en.wikipedia.org/wiki/File:Pipe-PFR.svg.

[36] Cantera Developers, *Plug flow reactor with surface chemistry*, https://cantera.org/dev/examples/python/reactors/surf_pfr.html, Accessed: 2025-05-28, 2025.

[37] OpenFOAM Foundation, *Openfoam – the open source cfd toolbox*, https://www.openfoam.com/, Accessed: May 28, 2025, 2025.

[38] J. Robledo Asencio, R. I. Savonov, and R. Intini Marques, "An open-source solver to model the catalytic decomposition of monopropellants for space thrusters", *Journal of Aerospace Technology and Management*, vol. 12, e1120, 2020, ISSN: 2175-9146. DOI: 10.5028/jatm.v12.1111. [Online]. Available: https://doi.org/10.5028/jatm.v12.1111.

[39] D. N. Nguyen, J. H. Lee, and C. S. Yoo, "Surfacechemistrymodels: A new library for simulations of reacting flows using surface reactions in openfoam", Manuscript in preparation, 2024.

[40] F. Wéry, L. A. Vandewalle, G. J. Heynderickx, and K. M. Van Geem, "Catchy-cfdem: Open-source microkinetic modeling of heterogeneous catalysis in eulerian-lagrangian cfd applied to oxidative coupling of methane", *Chemical Engineering Journal*, vol. 498, p. 155 247, 2024. DOI: 10.1016/j.cej.2024.155247. [Online]. Available: https://doi.org/10.1016/j.cej.2024.155247.

[41] V. M. Janardhanan and O. Deutschmann, "Cfd analysis of a solid oxide fuel cell with internal reforming: Coupled interactions of transport, heterogeneous catalysis and electrochemical processes", *Journal of Power Sources*, vol. 162, no. 2, pp. 1192–1202, 2006. DOI: 10.1016/j.jpowsour.2006.07.013.

[42] T. P. Coffee and J. M. Heimerl, "Transport algorithms for premixed, laminar steady-state flames", *Combustion and Flame*, vol. 43, pp. 273–289, 1981. DOI: 10.1016/0010-2180(81)90027-4.

[43] N. Realpe, S. R. Kulkarni, J. L. Cerrillo, *et al.*, "Modeling-aided coupling of catalysts, conditions, membranes, and reactors for efficient hydrogen production from ammonia", *React. Chem. Eng.*, vol. 8, pp. 989–1004, 4 2023. DOI: 10.1039/D2RE00458H. [Online]. Available: https://pubs.rsc.org/en/content/articlelanding/2023/re/d2re00458h.

[44] C. G. H. Jr. and J. M. Root, *An Introduction to Chemical Engineering Kinetics & Reactor Design*, 2nd. John Wiley & Sons, 2014.

[45] *Diffusion limitation - an overview | sciencedirect topics*, https://www.sciencedirect.com/topics/mathematics/diffusion-limitation, Accessed: 2025-06-27, 2025.

[46] J. R. García, C. M. Bidabehere, and U. Sedran, "Impact of the non-uniform catalyst particle size on product selectivities in consecutive reactions", *Catalysts*, vol. 12, no. 10, p. 1214, 2022. DOI: 10.3390/catal12101214. [Online]. Available: https://www.mdpi.com/2073-4344/12/10/1214.

[47] R. B. Bird, W. E. Stewart, and E. N. Lightfoot, *Transport Phenomena*, 2nd. John Wiley & Sons, 2002.

Appendix A Cantera script for ruthenium and nickel catalyst comparison

```python
import numpy as np
import matplotlib.pyplot as plt
import cantera as ct

# Constants and conversions
cm = 0.01
minute = 60.0
area = 100 * cm**2
length = 10 * cm
cat_area_per_vol = 1000.0 / cm
porosity = 1.0
velocity = 1.0  # m/s
temperature = 800 + 273.15  # K
pressure = 1 * ct.one_atm

# Catalyst 1 (Ru)
gas_Ru = ct.Solution(r"C:\Users\Hp\Desktop\Catlayst PFR\Ru_Published\
    Ru_Zhang.yaml", "gas")
surf_Ru = ct.Interface(r"C:\Users\Hp\Desktop\Catlayst PFR\Ru_Published\
    Ru_Zhang.yaml", "Ru_surface", [gas_Ru])
gas_Ru.TPX = temperature, pressure, 'NH3:1,H2:0,N2:0'
surf_Ru.TP = temperature, pressure
```

```
21
22 # Catalyst 2 (Ni)
23 gas_Second = ct.Solution(r"C:\Users\Hp\Desktop\Catlayst PFR\Nickel_NH3\
       nickel_ammonia.yaml", "gas")
24 surf_Second = ct.Interface(r"C:\Users\Hp\Desktop\Catlayst PFR\
       Nickel_NH3\nickel_ammonia.yaml", "Ni_surface", [gas_Second])
25 gas_Second.TPX = temperature, pressure, 'NH3:1,H2:0,N2:0'
26 surf_Second.TP = temperature, pressure
27
28 catalysts = [("Ru Catalyst", gas_Ru, surf_Ru), ("Ni Catalyst",
       gas_Second, surf_Second)]
29 conversion_results = {}
30
31 plt.figure()
32
33 for catalyst_name, gas, surf in catalysts:
34     mass_flow_rate = velocity * gas.density * area * porosity
35     reactor = ct.FlowReactor(gas)
36     reactor.area = area
37     reactor.surface_area_to_volume_ratio = cat_area_per_vol * porosity
38     reactor.mass_flow_rate = mass_flow_rate
39     reactor.energy_enabled = True
40
41     rsurf = ct.ReactorSurface(surf, reactor)
42     sim = ct.ReactorNet([reactor])
43
44     initial_NH3_X = gas.X[gas.species_index('NH3')]
45
46     distances = []
47     conversions = []
48
49     try:
50         while sim.distance < length:
51             sim.step()
```

```
52              current_NH3_X = reactor.thermo.X[reactor.thermo.
                    species_index('NH3')]
53              conversion_rate = (initial_NH3_X - current_NH3_X) /
                    initial_NH3_X
54              distances.append(sim.distance / cm)
55              conversions.append(conversion_rate)
56
57          plt.plot(distances, conversions, label=catalyst_name)
58
59      except Exception as e:
60          print(f"Simulation failed for {catalyst_name}: {e}")
61
62  plt.xlabel('Reactor Length (cm)')
63  plt.ylabel('Ammonia Conversion Rate')
64  plt.title(f'Ammonia Conversion along Reactor Length at {temperature} K,
      {velocity} m/s')
65  plt.legend()
66  plt.grid()
67  plt.savefig('Catalyst_Conversion_vs_Length.png')
68  plt.show()
```